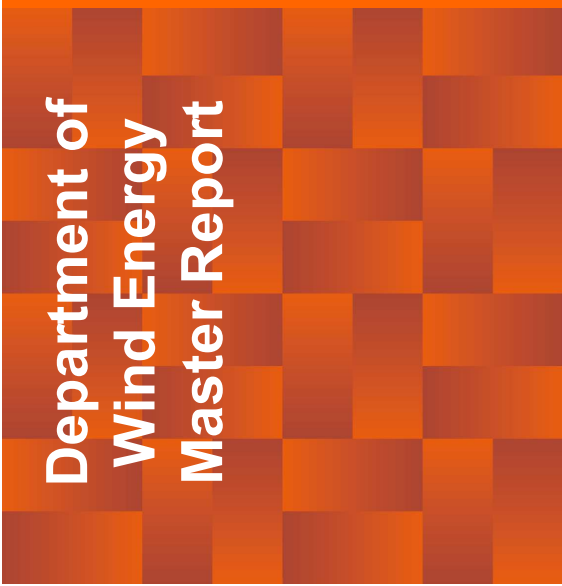


Conditional Error Statistics for Offshore Winds, from WRF Modelling and ASCAT Satellite Data



Department of
Wind Energy
Master Report

Stefano Ribaudo

DTU Wind Energy-M-0307

June 2019



DTU Wind Energy
Department of Wind Energy

Author: Stefano Ribaudo

Title: Conditional Error Statistics for Offshore Winds, from WRF
Modelling and ASCAT Satellite Data

DTU Wind Energy-M-03077

June 2019

Project period:

January 2019 – June 2019

ECTS: 30

Education: Master of Science

Supervisors:

Mark C. Kelly

Ioanna Karagali

Andrea N. Hahmann

DTU Wind Energy

Remarks:

This report is submitted as partial fulfillment of the requirements for graduation in the above education at the Technical University of Denmark.

DTU Wind Energy is a department of the Technical University of Denmark with a unique integration of research, education, innovation and public/private sector consulting in the field of wind energy. Our activities develop new opportunities and technology for the global and Danish exploitation of wind energy. Research focuses on key technical-scientific fields, which are central for the development, innovation and use of wind energy and provides the basis for advanced education at the education.

We have more than 240 staff members of which approximately 60 are PhD students. Research is conducted within nine research programmes organized into three main topics: Wind energy systems, Wind turbine technology and Basics for wind energy.

Technical University of Denmark

Department of Wind Energy
Frederiksborvej 399
2800 Kgs. Lyngby
Denmark

www.vindenergi.dtu.dk

Preface

The aim of this thesis is to provide a deeper understanding of the error statistics of WRF models with regard to the Advanced Scatterometer (ASCAT) measurements for the North Sea region, more precisely we'll look at conditional statistics of mentioned errors. Throughout the thesis we'll compare different WRF runs (called *ensembles* or *ensemble member*) based on their statistics. Since the ensembles may differ from each other for few key elements (called *schemes*), we can infer how the schemes are responsible for the errors. While information about the errors can be used directly to define the model uncertainty, information about different schemes can help decision making for research purposes.

I would like to personally thank my supervisors Mark C. Kelly, Ioanna Karagali and Andrea N. Hahmann for the help, skillful knowledge and patience shown during this five months of collaboration. I would also like to thank my family for their constant support and my elementary school math teacher Ada, to which I ultimately owe my interest in science.

Kongens Lyngby, 28-June-2019



Stefano Ribaudo

Abstract

Following the findings of Hahmann et al. (2015) we observe a bias in WRF simulations when compared to anemometer or Lidar measurements in the North Sea. This bias is expressed as the difference between average WRF model output and average measurements. This thesis's objective is to define and analyze WRF *error metrics* against ASCAT satellite data over the North sea and at 10 m height.

Initially we'll look at how the data is handled and converted through interpolation to enable the comparison. This will allow for the computation of the statistics that will help us determine how well the WRF model represents the measurements.

The statistical analysis begins with the analysis of marginal pdf for the variables of wind speed, wind direction and inverse Obukhov length for the WRF data. The subsequent conditional statistics will be performed conditioning over these variables.

Two different error metrics are defined, with the *raw error* representing the correspondence between individual simulations and measurements while the *time averaged error* represents the correspondence between average simulations and measurements.

Initially the presence and effects of phase shift for WRF simulations over the error metrics is investigated. The conditional analysis continues by conditioning the error metrics over WRF wind speed, wind direction and inverse Obukhov length.

A correction for the ASCAT wind speed is presented and new conditional statistics are obtained with the comparison against the corrected data.

Contents

Preface	i
Abstract	iii
1 Introduction	1
2 Data	3
2.1 ASCAT data	3
2.1.1 The ASCAT instrument	3
2.1.2 ASCAT data overview	4
2.2 WRF data	5
2.2.1 Introduction to the WRF model and model setup	6
2.2.2 WRF data overview	8
2.2.3 Selected area of interest	9
2.3 Grid interpolation	9
2.3.1 Grid selection	10
2.3.2 Interpolation of ASCAT data onto the WRF grid	11
2.3.3 Aggregation and interpolation of WRF data onto the AS-CAT grid	12
2.3.4 Choice of interpolation grid	14
2.3.5 Interpolation method	15
2.4 Time interpolation	19
3 Statistical analysis	21
3.1 Marginal statistics	21
3.1.1 Marginal statistics of wind speed	21
3.1.2 Marginal statistics of wind direction	22
3.1.3 Marginal statistics of inverse Obukhov length	23
3.2 Conditional statistics	25

3.2.1	Definition of ‘error’ metrics	26
3.2.2	Conditioning over correlation	26
3.2.3	Conditioning over wind speed	35
3.2.4	Conditioning over inverse Obukhov length	39
3.2.5	Conditioning over wind direction	42
3.3	Correction of ASCAT data	48
3.4	Conditional statistics with stability corrected ASCAT data . . .	52
4	Discussion	57
5	Conclusions	63
	Bibliography	67

CHAPTER 1

Introduction

With a total of 40 wind farms operating in the North Sea (as per 2015, Wikipedia (2015)) and the new planned wind farm *Thor* by the Danish energy ministry (EFKM, 2019), the North Sea is field of great interest for wind energy. To optimize the cost of energy, the location of a new wind farm must be taken in consideration during planning. The planning consists also of a wind resource assessment, in which the comparison between different possible sites based on the wind climate takes form. Along energy production, knowing the uncertainty of the wind climate is of great importance for both structural and economical reasons during planning (Nielsen, 2018).

Currently the estimation of wind resource offshore is done with numerical weather prediction models (NWP) rather than the alternatives of in situ measurements (which are expensive and available for a limited number of sites) or satellite based measurements (that may have larger uncertainties than in situ measurements) (Hahmann et al., 2015).

The Weather, Research and Forecast model (WRF) (Skamarock et al., 2008) is one of such NWP models and includes a wide range of *physics options* or *schemes* that govern the physical interactions within the simulations. This model is used for the NEWA project, which aims to the creation and publication of a state of the art electronic European wind atlas based on WRF simulations (Karagali et al., 2018). Moreover, the NEWA project established different experiments to evaluate the model sensitivity to different schemes offshore. The performance of these simulations is assessed with comparison to ASCAT winds. Given the premises described, throughout this thesis we'll analyze different WRF simulations for the North sea.

The simulated wind speeds for each ensemble member will be compared with measurements from the ASCAT satellite data, by applying *error metrics* specifically adapted for this study. The definition and analysis of the error metrics is carried out both to offer results comparable with other literature in the field and to help the reader define its own error metric by understanding the information that one could infer from it. The latter concept is expanded with the use of conditional statistics, that will help study the error metrics dependencies on major variables of interest for wind energy applications and meteorology research. Initially we'll condition on correlation between WRF and ASCAT data to study the effects of phase shift (Rosgaard, 2015). The conditioning over wind speed follows a typical power curve of a wind turbine and is intended to show the model performance for energy production purposes. Conditioning the error metrics over inverse Obukhov length shows the model performance over different atmospheric conditions and conditioning over wind direction was initially intended for testing purposes but instead yielded interesting results.

Following the results obtained while conditioning over atmospheric stability, a stability correction for the ASCAT data is implemented. This correction allowed for the discerning of errors given by the WRF simulations from those caused by the assumption of neutral atmospheric conditions for the ASCAT data.

From the results obtained we'll be able to analyze the performance of the simulations both from a physical point of view and from a scheme to scheme comparison. The latter could be used to define ensemble members with specific objectives, such as the minimization of an error metric. Given that the reader is interested in the error metrics presented, one could also derive the model uncertainty over such error metrics.

CHAPTER 2

Data

2.1 ASCAT data

A brief description of the ASCAT instrument is presented in the next section, followed by a general overview of the data used. The data is available from the year 2015.

2.1.1 The ASCAT instrument

The data is acquired by two satellites platforms, Metop-A and Metop-B. The ASCAT instrument consists a pair of three antennas, one for each side of the satellite. These antennas measure the back-scattering from the water surface. The measured signal is called radiometrically-calibrated Level 1b NRCS, or σ_0 . This signal is then converted with a empirical Geophysical Model Function (GMF) that relates σ_0 , wind speed, direction and signal incident angle (EUMETSAT, 2015). The measurement swath and difference between the right and left group of antennas is visible in figure 2.2, where for example the two green stripes represent the two swaths. The latter are about 550 km wide. Note that the ASCAT instrument data is converted to wind speeds assuming neutral atmospheric conditions (p. 39, EUMETSAT, 2015).

2.1.2 ASCAT data overview

The ASCAT data were obtained from the E.U. Copernicus Marine Service Information and analyzed by DTU Wind Energy (Copernicus, 2017).

The analyzed data comes in .mat files, one for each day. These have a resolution of 0.125 degrees in both longitude and latitude. Each file is comprised of four passes. Each pass can be ascending or descending for either one of the satellites platforms, and throughout this thesis each individual pass will take the name of *ASCAT temporal snapshot*.

Throughout this thesis the ASCAT data always refers to the height of 10 m above mean sea level.

Figure 2.1 shows an example of ASCAT data. The figure shows the ascending pass of Metop-A for the first of January 2015. As we can see the data looks striped due to the instrument measurement swaths. Further analysis is presented in figure 2.2.

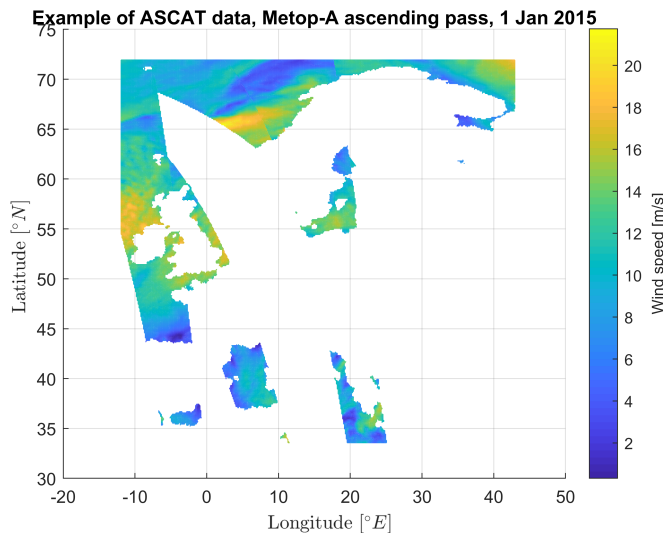


Figure 2.1: An example of ASCAT data, showing wind speed. This figure presents the data obtained by Metop-A on the ascending pass on the 1st of January 2015. Since this data comes from one satellite and one specific pass, the data shown takes the name of *ASCAT temporal snapshot*.

From figure 2.2 we can see that for a single ASCAT temporal snapshot we have

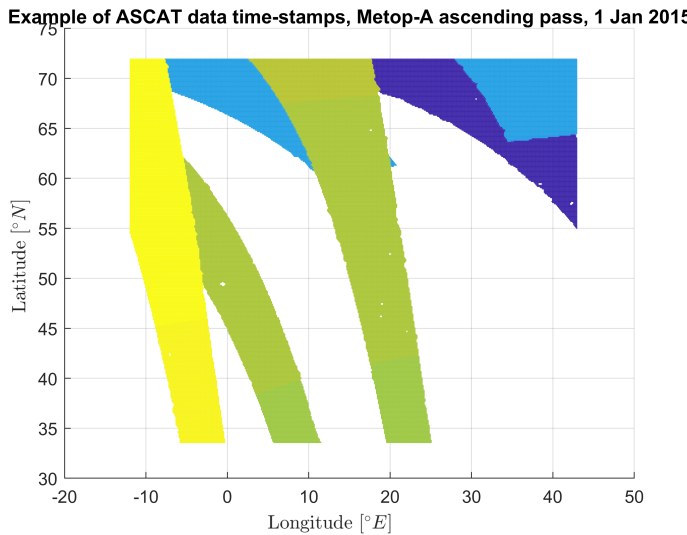


Figure 2.2: An example of ASCAT data, showing the wind speed measurement time. This figure presents the data obtained by Metop-A on the ascending pass on the 1st of January 2015. Each color represents a different measurement time. The approximate measuring time for the colors presented are (in ascending order): dark blue (~16:54), light blue (~18:35), green (~20:11) and yellow (~21:52).

measurements at different times, from around 16:54 for the dark blue area to around 21:52 for the yellow area. The measurement time is not uniform for the same color, e.g. the green area presents measurements from 20:05 at Latitude 34° N to 20:17 at Latitude 72° N. Figure 2.2 also shows that subsequent measurements overwrite previous measurements in our data.

These considerations will be of practical use later for both computing the correlation coefficient between ASCAT and WRF data and the process of time interpolation.

2.2 WRF data

The WRF data used throughout this thesis is stored on the *neweuropeanwindatlas.eu* servers and part of the NEWA project (Karagali et al., 2018). Data from two domains is used, the North sea domain (NW domain in the NEWA project, figure 2.3) and the UK domain (figure 2.4).

The UK data was downloaded manually and will be used to analyze the performance of the interpolation methods. This data was initially used due to a time delay for the North sea domain data. The data for the North Sea domain was directly handed by DTU Wind Energy and consists of 9 ensembles. Analogously to the ASCAT data, all the data used refers to the year 2015.

The data comes in .nc files and is stored using a NetCDF data format (Wikipedia, 2019). This specific data format has been accessed to using the NetCDF library in Matlab (MathWorks, 2019).

2.2.1 Introduction to the WRF model and model setup

The WRF model (Weather Research and Forecasting Model) is a meso-scale numerical prediction system and it is used for a wide range of research and operational applications (Skamarock et al., 2008).

The WRF model is used with a series of *schemes* and *physical options* that will parameterize the physical interactions within the simulation. A detailed list of schemes can be found on the [UCAR official web page](#) (UCAR, 2019).

Each ensemble member analyzed will have a unique combination of schemes and will be identified with the names of the schemes used. Our ensemble members differ for the choice of four schemes: the PBL (planetary boundary layer) scheme, the surface layer scheme, the SST (surface sea temperature product used for initial conditions) and the land surface scheme. A list of the adopted schemes is presented in table 2.1.

Scheme category	Scheme names
PBL	ACM (Pleim, 2007) MYJ (Janji, 1994) MYNN (Nakanishi and Niino, 2006) YSU (Hu et al., 2013)
Surface layer	PX (Noilhan and Planton, 1989) MO (Monin and Obukhov, 1954) MM5 (Jimnez et al., 2012) MYNN
SST	OSTIA (Donlon et al., 2012) OISST (Reynolds et al., 2002)
Land surface	RUC (Benjamin et al., 2004) NOAH (Tewari et al., 2004)

Table 2.1: List of schemes used for the ensemble members

To each ensemble member we'll assign a name that is a composite name of the used schemes. The names will follow the pattern: PBL - Surface layer - SST - Land surface.

The WRF simulations are performed in a nested configuration, where the outer domain drive the inner domain. The outer domain is initialized with lateral boundary conditions from the atmospheric reanalysis ERA Interim, with resolution $0.75^\circ \times 0.75^\circ$ (Dee et al., 2011). Figure 2.3 presents various domains used in the latest NEWA report where the yellow domain corresponds to the North Sea domain analyzed through this thesis (Witha et al., 2019).

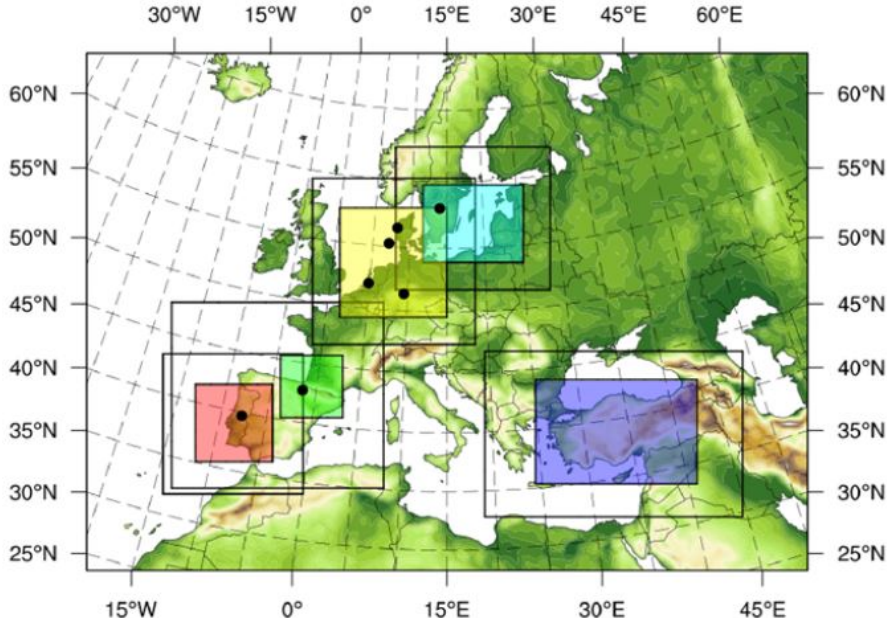


Figure 2.3: Map showing the WRF domains used in the latest NEWA report (Witha et al., 2019). The North Sea domain analyzed in this thesis is presented in yellow (formally known as NW in the NEWA report). The dots represent measuring stations whose data is unavailable for this thesis. The surrounding black rectangles represent the outer domains.

The UK domain is shown in figure 2.4 and represented by the initials GB.

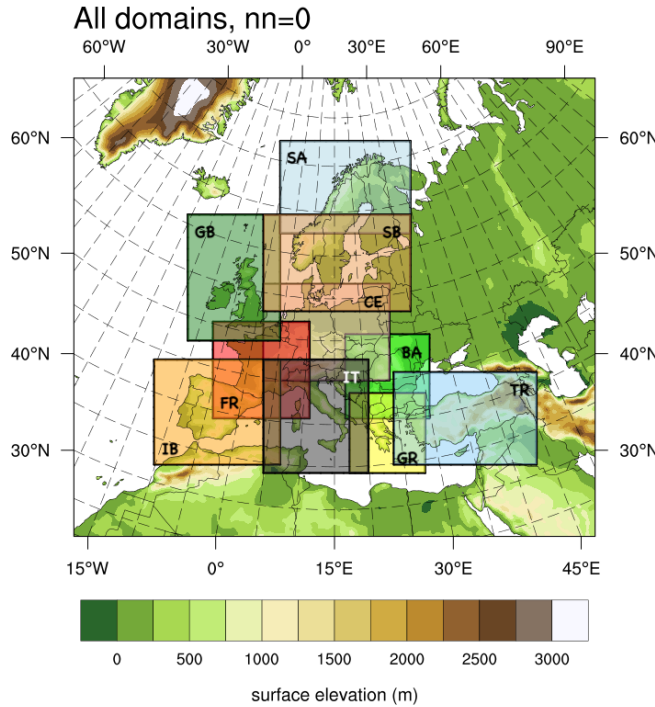


Figure 2.4: Map showing domains for the WRF run that produced the UK data. The UK domain is represented by the initials GB.

2.2.2 WRF data overview

The data is divided into square grid cells of 9 km^2 , and the grid cells centers have a spatial resolution of 3 km. The temporal resolution is 30 min, or 48 values per grid cell per day.

With *WRF temporal snapshot* we refer to the collection of values for a variable given a fixed point in time and an ensemble member. An example is given in figure 2.5. For wind speed and direction, the WRF data used for this thesis refers to the height of 10 m above mean sea level.

2.2.3 Selected area of interest

Since the NW domain shown in figures 2.5 and 2.3 is comprised of both sea and land grid points, we define a new area of interest that covers only sea grid points. Only grid points further than 50 km to coastal grid points have been chosen to avoid the transitional inner boundary layer due to surface roughness change (p. 132, Berg et al., 2017). The area will also be at least 30 km away from the domain borders due to the nested setup. Figure 2.5 presents the grid points selected, where the area is centered at longitude 4.08 [$^{\circ}$ N] and latitude 55.85 [$^{\circ}$ E]. This selected area measures 186300 km^2 and spawns 414 km horizontally and 450 km vertically.

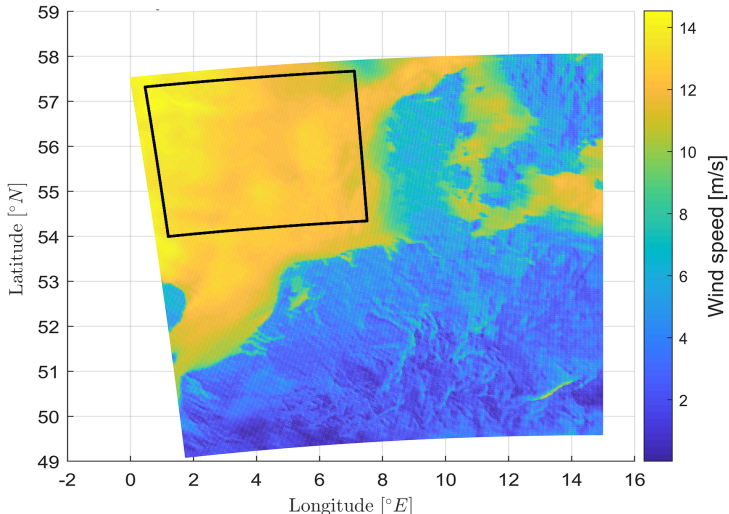


Figure 2.5: An example of WRF data, showing the wind speed. This data refers to the ensemble member MYNN-MYNN-OSTIA-NOAH for the 1st of January 2015 at 00:00. The selected area is delimited by black lines.

2.3 Grid interpolation

Since ASCAT and WRF data comes for different points in space and at different times, the first step in our analysis is to define an interpolation procedure to be able to align ASCAT and WRF data in both space and time. Doing so will

allow us to compare the two different data in a meaningful way. To interpolate in space we have different options:

- We could interpolate the ASCAT data on the WRF grid or vice versa;
- We must chose an interpolation method, e.g. linear / cubic etc...

To analyze to which choice is better for our study, we introduce the concept of interpolation error. This is to express the consequences of any interpolation we wish to adopt. For this study two parameters are chosen as representative of the interpolation error: the difference in average wind speed and the ratio of wind speed variance. Both quantities are computed from the wind speed field prior and after the interpolation, and each time we interpolate.

The difference in average wind speed is chosen to test whether the interpolation overpredicts the highest (or lowest) wind speeds and underpredicts the lowest (or highest) wind speeds. This choice is an adaptation of the guidelines presented in p 44, Li and Heap (2008). The closer this parameter is to 0, the highest the performance of the interpolation.

$$\Delta_{Ai} = \langle U_{i, \text{WRF grid}} \rangle_{x,y} - \langle U_{i, \text{ASCAT grid}} \rangle_{x,y} \quad (2.1)$$

The subscript i in equation 2.1 indicates the temporal snapshot i .

The ratio of wind speed variance is chosen to test if the interpolation over predicts (or under predicts) the extremes (both high and low). This choice is presented in p 44, Li and Heap (2008), and is the optimal measurement of performance that we can use from this source. This parameter shows a better performance the closer it gets to 1.

$$RVAR_i = \frac{VAR[U_{i, \text{WRF grid}}]}{VAR[U_{i, \text{ASCAT grid}}]} \quad (2.2)$$

Again the subscript i indicates the temporal snapshot i and VAR is the statistical variance.

2.3.1 Grid selection

We can interpolate the ASCAT data on the WRF grid or we can interpolate the WRF data on the ASCAT grid.

Generally speaking, it is recommended to interpolate data from the finer grid (WRF grid) to the coarser grid (ASCAT grid) (p. 357, Wilks, 2011).

In our case this means to interpolate WRF data to the ASCAT grid.

Although this recommendation may be true for most cases, we've spotted possible problems for both approaches and no one given solution looks better than the other without a proper analysis of the options.

Specifically, if we were to interpolate the ASCAT data onto the WRF grid we would introduce new, unmeasured data. This is due to the WRF grid being finer than the ASCAT grid.

If we were to interpolate the WRF data onto the ASCAT grid we will leave some of the predictor points out from the computation. This is since the interpolation methods presented further will use a finite set of neighbouring points to predict. Given the differences in grids, many points on the WRF grid are not neighbouring any ASCAT grid point. For the North sea selected area (figure 2.5), it is computed that approximately 26% of the WRF grid points will be used for a bilinear interpolation, leaving the remaining 74% of the data unrepresented (computation not shown). This effect is less prominent the lower the wind speed gradient in our wind fields. Fortunately, we'll analyze sea areas for which the wind speed gradient is generally lower than on land.

2.3.2 Interpolation of ASCAT data onto the WRF grid

To measure the performance of this interpolation we'll use the parameters expressed in equations 2.1 and 2.2. The data labeled as *ASCAT grid* refers to the original data, while *WRF grid* refers to the interpolated data.

We'll compute these parameters for every time we apply the interpolation. The next figures show the distribution of such parameters when computed for the whole year.

Looking at the mean of the distribution of Δ_A in figure 2.6 we can observe that the interpolation shows good performance. The standard deviation shows that the difference in average wind speed is generally confined in a ± 0.04 interval. This result is not ideal, although its relative importance will be contextualized further in the reading.

The distribution of *RVAR* shown in figure 2.7 presents a mean value slightly less than 1, indicating that the interpolation generally slightly under predicts the extremes of wind speed. Some information about the minimum and maximum of the wind field is therefore lost due to interpolation. The opposite is true when this ratio is more than 1, where the interpolation over predicts the extremes. Given the distribution shown, the latter is less likely.

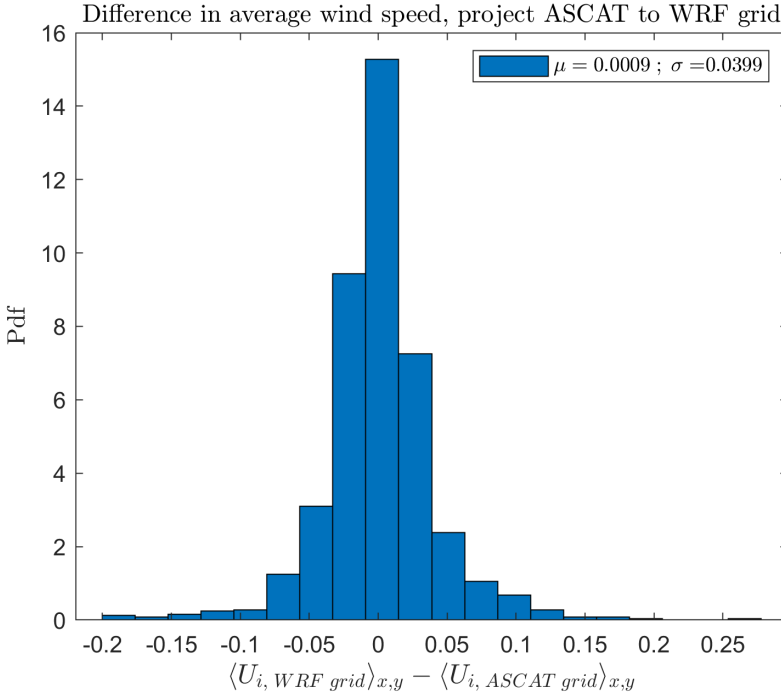


Figure 2.6: Distribution for the interpolation error metric *difference in average wind speed* for the ASCAT data. The ASCAT data on its original grid is denoted as $U_i, \text{ASCAT grid}$ while the interpolated ASCAT data on the WRF grid is denoted as $U_i, \text{WRF grid}$. The subscript i refers to the temporal snapshot number. Mean and standard deviation for the distribution are shown in the upper-right corner. The interpolation method is bilinear.

2.3.3 Aggregation and interpolation of WRF data onto the ASCAT grid

The interpolation performance is again measured as in previous section. This analysis is performed using data from the MYNN-MYNN-OSTIA-NOAH ensemble member. Since we'll use equations 2.1 and 2.2 as presented, the data labeled as *ASCAT grid* refers to the interpolated data, while *WRF grid* refers to the original data. This will change the interpretation of our performance parameters. This is particularly true for *RVAR*.

The mean and standard deviation of the difference of averages in figure 2.8 are

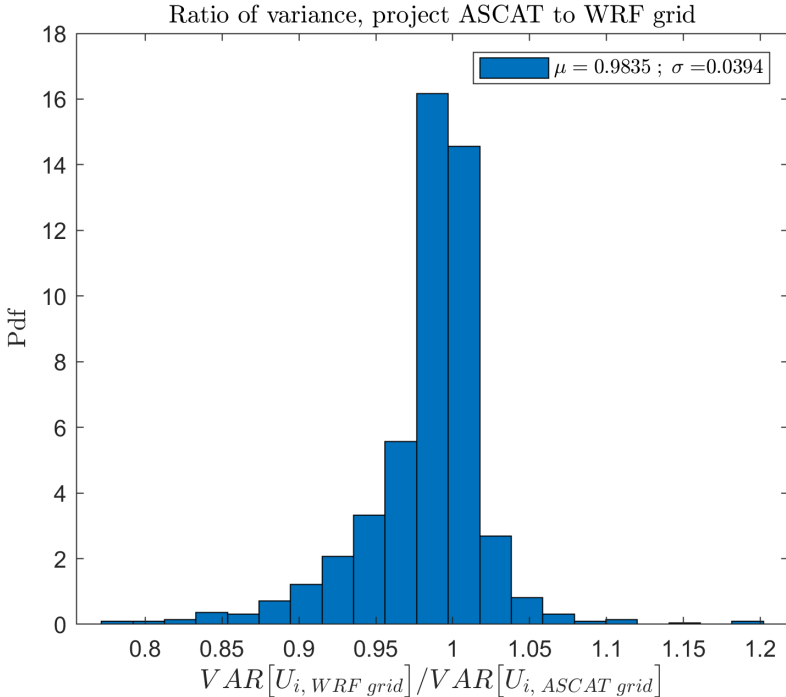


Figure 2.7: Distribution for the interpolation error metric *ratio of variance* for the ASCAT data. The ASCAT data on its original grid is denoted as $U_i, \text{ASCAT grid}$ while the interpolated ASCAT data on the WRF grid is denoted as $U_i, \text{WRF grid}$. The subscript i refers to the snapshot number. Mean and standard deviation for the distribution are shown in the upper-right corner. The interpolation method is bilinear.

comparable with those for the other interpolation choice in figure 2.6. The standard deviation of Δ_A looks slightly bigger when interpolating the WRF data onto the ASCAT grid, reflecting the effect for which not all the WRF data is used within the interpolation. Due to this effect, it will randomly happen that some of our interpolations are computed with higher than average (or lower than average) wind speeds and therefore will over predict (or under predict) the wind field average. Regarding the ratio of variance $RVAR$ presented in figure 2.9, the mean of its distribution is slightly higher than 1 indicating that again the act of interpolation generally loses information about the extremes of the wind field. The standard deviation of this distribution is comparable with the other interpolation choice in figure 2.7.

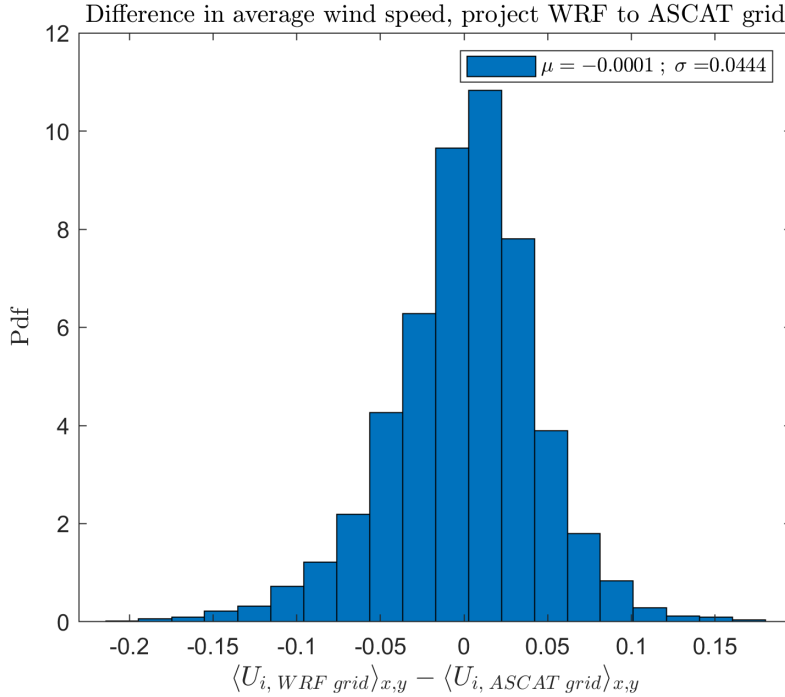


Figure 2.8: Distribution for the interpolation error metric *difference in average wind speed* for the WRF data. The WRF data on its original grid is denoted as $U_i, \text{WRF grid}$ while the interpolated WRF data on the ASCAT grid is denoted as $U_i, \text{ASCAT grid}$. The subscript i refers to the snapshot number. Mean and standard deviation for the distribution are shown in the upper-right corner. The interpolation method is bilinear.

2.3.4 Choice of interpolation grid

Given the results presented in the previous sections, it looks like interpolating the ASCAT data onto the WRF grid is the choice that allows for the highest interpolation performance. This is based on the standard deviations for the difference in averages in figures 2.6 and 2.8 (0.0399 and 0.0444 respectively), with the interpolation of ASCAT data to WRF grid showing the smallest value. This is also based on the means for the ratio of variance in figures 2.7 and 2.9 (0.984 and 1.052 respectively), with the interpolation of ASCAT data to WRF grid showing the closest value to 1.

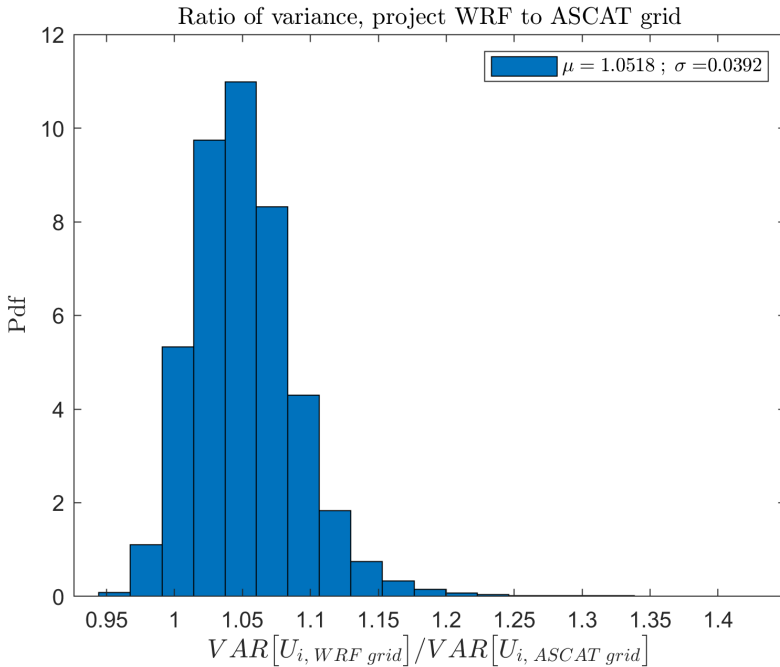


Figure 2.9: Distribution for the interpolation error metric *ratio of variance* for the WRF data. The WRF data on its original grid is denoted as $U_i, \text{WRF grid}$ while the interpolated WRF data on the ASCAT grid is denoted as $U_i, \text{ASCAT grid}$. The subscript i refers to the snapshot number. Mean and standard deviation for the distribution are shown in the upper-right corner. The interpolation method is bilinear.

Having knowledge of the later sections, the difference in performance is not as important as other considerations. This means that the suggestion in *Statistical methods in the atmospheric sciences, third edition* based on the choice of interpolation grid alone does not find justification for this thesis. (p. 357, Wilks, 2011)

2.3.5 Interpolation method

By *interpolation method*, we refer to the algorithm used to perform the interpolation. Due to the complexity of such algorithms we prefer to use a stan-

dard Matlab function called `griddata` (Mathworks, 2019a). The only choices of method that this function allows that could be useful for our study are `bilinear` and `bicubic`. Having presented the problems when interpolating the WRF data onto the ASCAT grid, it is of doubt if a method that uses more predictor points performs better. For clarity a bicubic method always uses more predictor points than bilinear. (Mathworks, 2019b)

Since this study was performed on the UK domain and showed definitive results, we are not going to replicate it for the North sea area. Specifically, only the sea grid points at least 6 km away from the coast were taken into consideration. This study was also only performed on the WRF data since we would expect a higher influence from the interpolation method than on the ASCAT data.

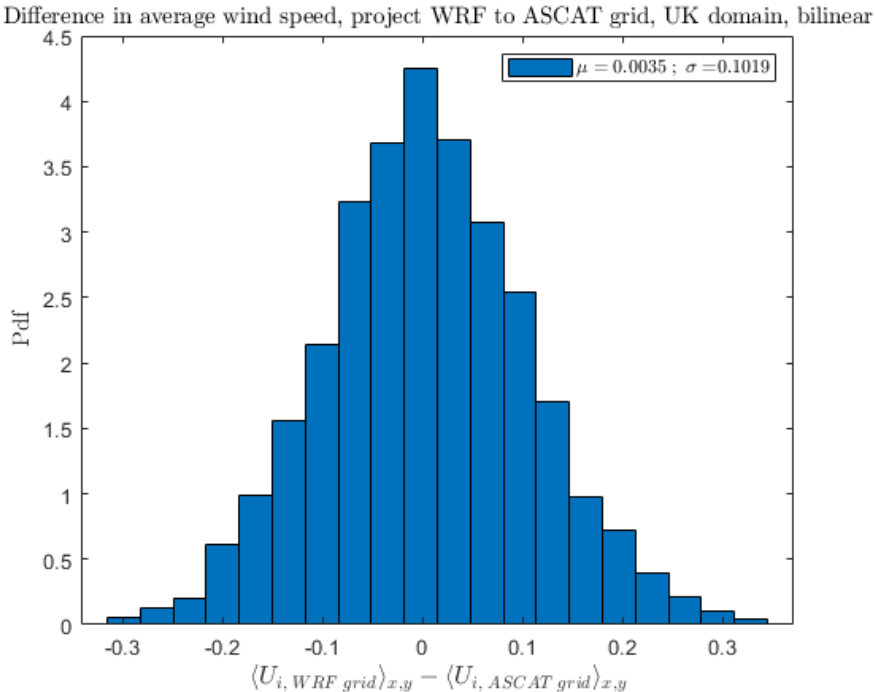


Figure 2.10: Distribution for the interpolation error metric *difference in average wind speed* for the UK data using bilinear method. The WRF data on its original grid is denoted as $U_i, WRF\ grid$ while the interpolated WRF data on the ASCAT grid is denoted as $U_i, ASCAT\ grid$. The subscript i refers to the snapshot number. Mean and standard deviation for the distribution are shown in the upper-right corner.

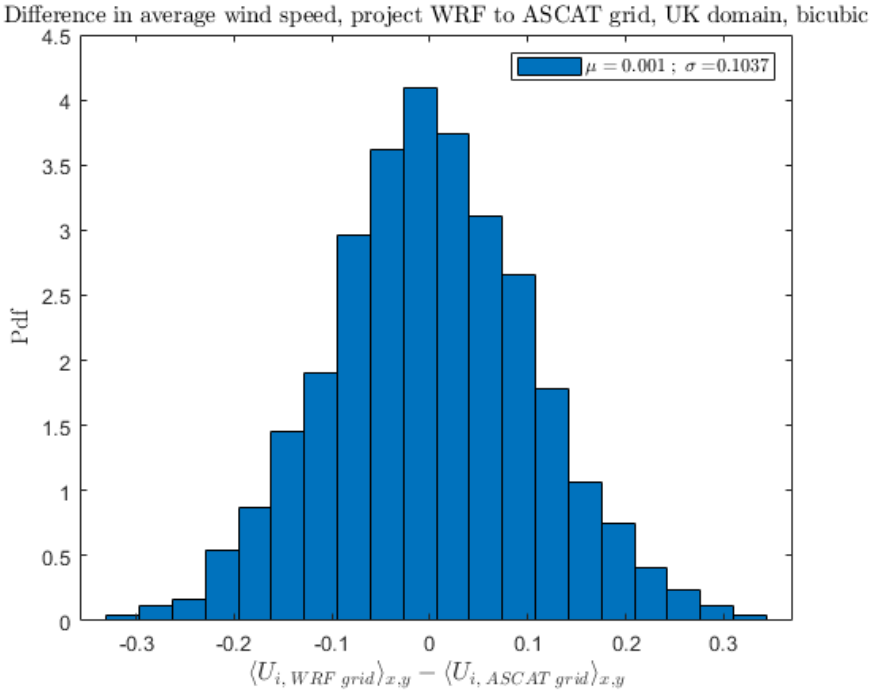


Figure 2.11: Distribution for the interpolation error metric *difference in average wind speed* for the UK data using bicubic method. The WRF data on its original grid is denoted as $U_i, WRF\ grid$ while the interpolated WRF data on the ASCAT grid is denoted as $U_i, ASCAT\ grid$. The subscript i refers to the temporal snapshot number. Mean and standard deviation for the distribution are shown in the upper-right corner.

Figures 2.10 and 2.11 show the distribution of difference in average wind speed for the UK domain for bilinear and bicubic methods respectively. The distributions present similar mean and standard deviation. The shape of the distributions visually look very similar and Gaussian distributed.

Figures 2.12 and 2.13 show the distributions of ratio of variance for the UK domain for bilinear and bicubic methods. Again the distribution look alike, with very similar mean and standard deviation.

Given the absence of significant difference between the two interpolation methods, the bilinear method is preferred due to lower computational time.

Given the similarities between the grids for WRF data on UK and North Sea domains we would expect to obtain analogous results for the WRF data on the

North Sea domain.

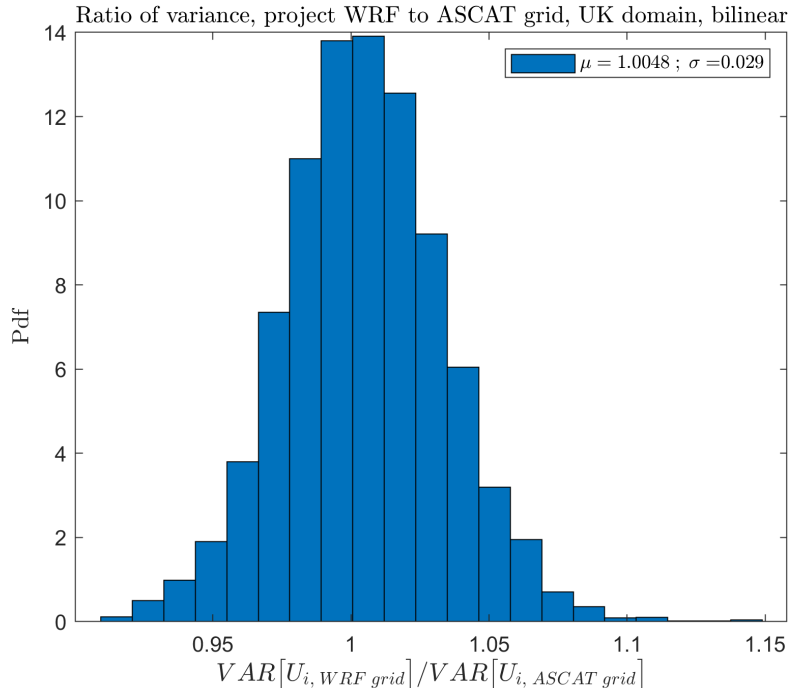


Figure 2.12: Distribution for the interpolation error metric *ratio of variance* for the UK data using bilinear method. The WRF data on its original grid is denoted as $U_i, \text{WRF grid}$ while the interpolated WRF data on the ASCAT grid is denoted as $U_i, \text{ASCAT grid}$. The subscript i refers to the temporal snapshot number. Mean and standard deviation for the distribution are shown in the upper-right corner.

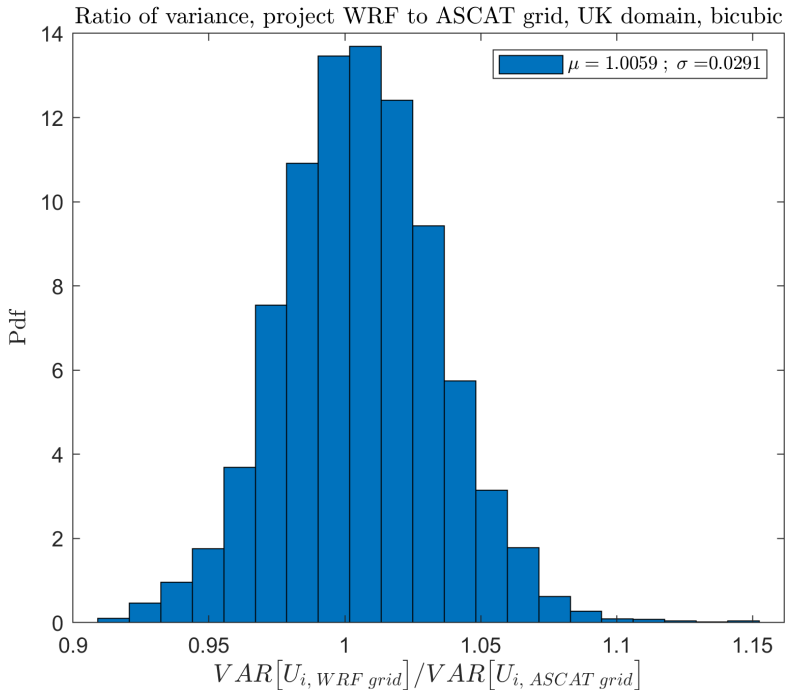


Figure 2.13: Distribution for the interpolation error metric *ratio of variance* for the UK WRF data using bicubic method. The WRF data on its original grid is denoted as $U_i, \text{WRF grid}$ while the interpolated WRF data on the ASCAT grid is denoted as $U_i, \text{ASCAT grid}$. The subscript i refers to the temporal snapshot number. Mean and standard deviation for the distribution are shown in the upper-right corner.

2.4 Time interpolation

With time interpolation we have again the choice of interpolating the ASCAT data onto the WRF time stamps or interpolating the WRF data onto the ASCAT time stamps, however in this case we only have one useful choice.

Due to how the ASCAT data is presented, we have a maximum of four measurements per grid point, and this data is most often available unevenly during the day.

On the other hand, the WRF data has reliable time stamps that are evenly distributed, one data point per half hour. This brings us to a total of 48 data

per grid point per day.

Due to the interpolation algorithm and these considerations projecting the WRF data onto the ASCAT time stamps is a far superior choice. (p. 57-58, Li and Heap, 2008)

CHAPTER 3

Statistical analysis

3.1 Marginal statistics

By *marginal statistic* we refer to statistics obtained without applying any condition, that is using all available data. (After interpolations and considering only the selected area in figure 2.5)

Marginal statistics will give us a basic understanding of the variables that we are going to analyze further with conditional statistics.

3.1.1 Marginal statistics of wind speed

In order to characterize the wind speed for the ASCAT data and the WRF ensemble members we are going to present the distributions of wind speed.

Figure 3.1 shows the marginal probability distribution function of wind speed for the ASCAT data, WRF ensemble members MYNN-MYNN-OSTIA-NOAH (base run, red line) and MYNN-MO-OSTIA-NOAH (production run, yellow line). The bin width for these distributions is about $0.34 [m \cdot s^{-1}]$. The distributions are plotted from the 0.01 quantile to the 0.99 quantile.

From figure 3.1 the differences between the ASCAT data and the ensembles are most noticeable in the ranges of wind speed from about $4.2 [m \cdot s^{-1}]$ to about $9 [m \cdot s^{-1}]$.

Both wind speed distributions from the ensemble members differ from the ASCAT wind speed distribution near the peak of the distribution and overestimate

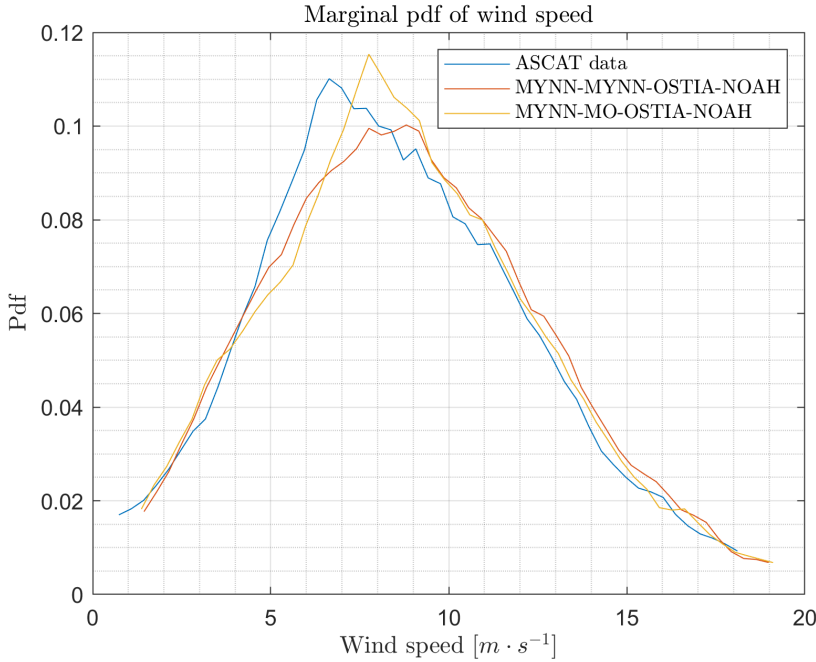


Figure 3.1: Marginal distributions of wind speed for the ASCAT data and the ensembles members MYNN-MYNN-OSTIA-NOAH and MYNN-MO-OSTIA-NOAH. The distributions are shown from the 0.05 quantile to the 0.95 quantile.

it.

Compared to each other, the production run overestimates wind speeds from 7.5 [m · s⁻¹] to 9 [m · s⁻¹], while the other ranges of wind speeds are underestimated.

The difference between the ensemble members can be traced to the surface layer scheme, MYNN for the base run and MO for the production run.

3.1.2 Marginal statistics of wind direction

To give a general understanding when conditioning on wind direction we present the probability of occurrence for each wind direction. Note that to facilitate the reading of subsequent plots, the wind direction has been divided into four intervals, one for each cardinal direction and spawning 90° each. The directions

are defined with 0° representing winds coming from North and 90° representing winds coming from East.

Figure 3.2 shows the probability of occurrence of wind directions for the ensemble member MYNN-MYNN-OSTIA-NOAH. The most common direction is West and followed by South, North and lastly East.

All the ensembles present a fairly similar behaviour for wind direction.

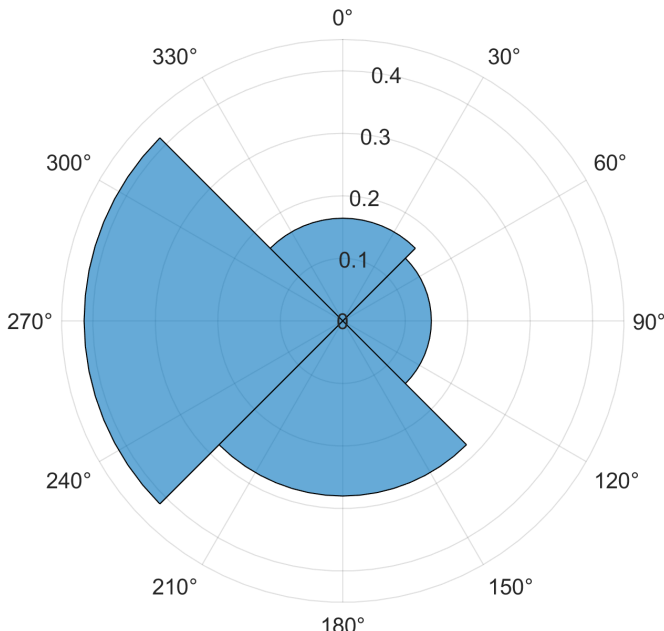


Figure 3.2: Probability of occurrence for wind direction, ensemble member is MYNN-MYNN-OSTIA-NOAH. Showing one sector per cardinal directions due to similarity with other figures.

3.1.3 Marginal statistics of inverse Obukhov length

The Obukhov length (Obukhov, 1971) can be interpreted as a measure of buoyancy. The atmospheric stability is related to buoyancy effects and therefore the the Obukhov length. Unstable atmospheric conditions are characterized by negative Obukhov length and stable atmospheric conditions when the

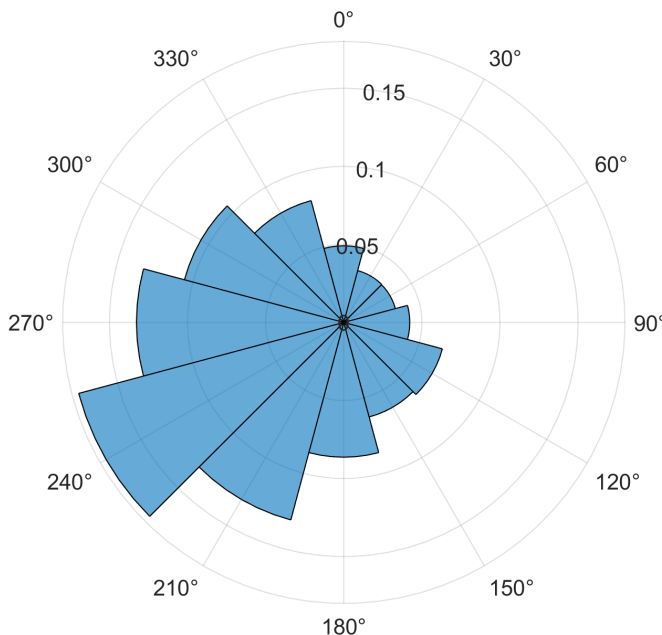


Figure 3.3: Probability of occurrence for wind direction, ensemble member is MYNN-MYNN-OSTIA-NOAH. Showing the commonly used 12 sectors.

Obukhov length is positive. Studying the atmospheric conditions with the inverse Obukhov length ($1/L$) is generally more convenient, and neutral atmospheric conditions are characterized when the latter value is close to 0 (Berg et al., 2017).

Figure 3.4 shows the marginal pdf of inverse Obukhov length for the ensemble member MYNN-MYNN-OSTIA-NOAH. The distribution presents a peak around zero and the tails are not symmetrical with the tail on the negative side being bulkier. This indicates that unstable conditions are more prominent than stable conditions as one can expect from the sea surface ¹.

¹The relative high heat capacity of water makes so that the water is still generally warmer than air overnight, keeping the heat flux directed towards the atmosphere and therefore creating unstable conditions. During the day both land and sea surfaces are generally warmer than the air due to the sun's heating.

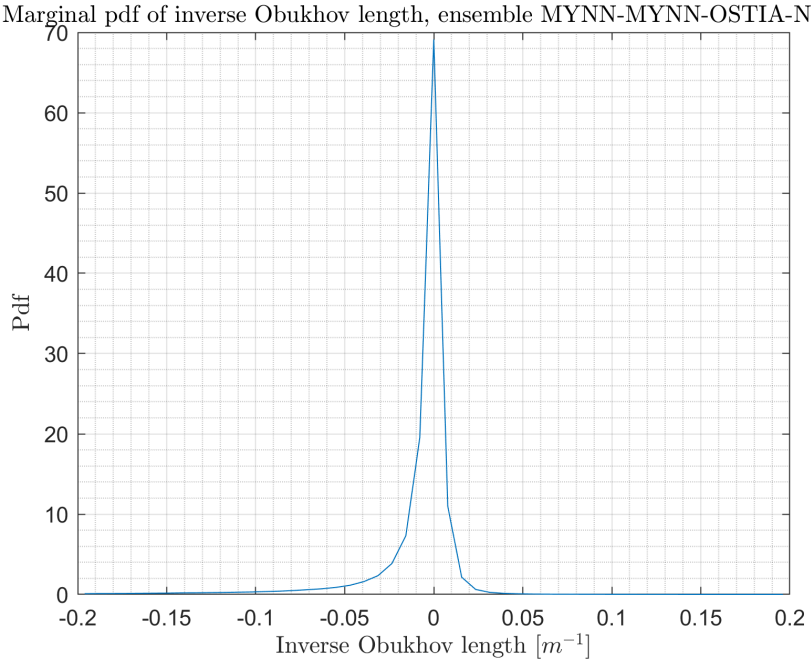


Figure 3.4: Marginal distribution of inverse Obukhov length for the ensemble MYNN-MYNN-OSTIA-NOAH. This typical shape is shared for all ensemble members.

3.2 Conditional statistics

By *conditional statistics* we refer to statistics obtained when analyzing only a fraction of the available data. (After interpolations and considering only the selected area in figure 2.5)

Following e.g. Pope (2000) or Berg et al. (2017) we define the conditional pdf of X given Y :

$$f(x | Y) \quad (3.1)$$

From a practical standpoint this is equivalent to compute the pdf of X selecting only values of X that were obtained when $y_0 < Y \leq y_1$.

As shown in later sections the values for y_0 and y_1 will be chosen to represent and isolate a defined event, such as stable atmospheric conditions or Easterly winds.

To give an additional perspective on the definition, the marginal pdf would be defined as in 3.1 with $-\infty < Y \leq +\infty$.

3.2.1 Definition of ‘error’ metrics

The objective of the WRF error metrics is to describe and summarize the differences between the wind speeds measured by the ASCAT satellites and the wind speeds simulated by a WRF ensemble member.

To this end we define the *raw error* and *time averaged error* respectively as:

$$RE|_{x,y,t} \equiv (U_w - U_a)|_{x,y,t} \quad (3.2a)$$

$$TAE|_{x,y} \equiv \left(\langle U_w \rangle_t - \langle U_a \rangle_t \right) \Big|_{x,y} \quad (3.2b)$$

Following the definitions in equations 3.2 we’ll have one raw error per measurement point and one time averaged error per grid point.

The time averaged error has been chosen as a *bias* metric, while the raw error has been chosen as an *accuracy* metric, with definitions of bias and accuracy as in p. 304, Wilks (2011).

More specifically, the *raw error* represents the correspondence between individual simulations and measurements while the *time averaged error* represents the correspondence between average simulations and measurements.

The choice for the TAE also reflects a possible error metric when evaluating the mean annual wind speed for a given grid cell.

These error metrics will be analyzed primarily in terms of mean and standard deviation. The mean can reveal any systematic difference, while the standard deviation gives information about how the error metric is consistently close to the mean value. The notation $\langle RE \rangle_{xy,t}$ indicates the mean of RE over all grid point and all times, while $\sigma_{RE_{xy,t}}$ indicates the standard deviation of RE over all grid points and all times. The analogous is true for TAE, but the subscript will be xy to indicate that the statistic is computed over all grid points.

3.2.2 Conditioning over correlation

One common problem with WRF runs is the presence of phase shift, for which the simulation can predict an event before or after its observation or at a slightly different coordinate.

Understanding this effect is the first objective of our analysis of WRF errors. This is to ensure that the differences between measurements and simulations is not due to a simple space and time mismatch.

The first step would be to find a quantity to describe the spatial mismatch between measurements and simulations. Pearson’s correlation coefficient has

been chosen to describe the correlation (p. 50, Wilks, 2011). An equivalent expression is presented below.

$$r_{AW} = \frac{1}{n-1} \sum_{i=1}^n \left(\frac{a_i - \mu_a}{\sigma_a} \right) \left(\frac{w_i - \mu_w}{\sigma_w} \right) \quad (3.3)$$

Where a represents the ASCAT wind speeds, w the WRF wind speeds, μ represents the mean, σ is the standard deviation and n is the sample size. Note that the Pearson's correlation coefficient is computed for each swath (figure 2.2) and is only a function of time. For clarity, $r_{AW} = +1$ implies a linear correlation between the two variables, which we interpret as no spatial mismatch. Figure 3.5 shows the distribution of correlation coefficient for the ensemble member MYNN-MYNN-OSTIA-NOAH, while figure 3.6 shows the mean correlation coefficient for each ensemble member.

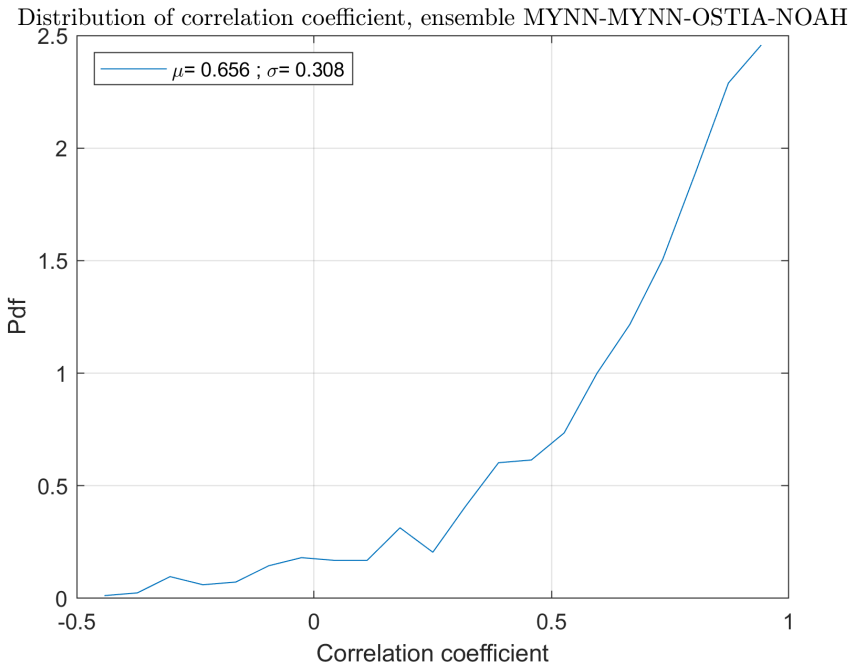


Figure 3.5: Distribution of Pearson's correlation coefficient for the ensemble member MYNN-MYNN-OSTIA-NOAH. Other ensemble members show a similar distribution, meaning that phase shift is observed for all simulations.

The distribution of correlation coefficient in figure 3.5 shows that the mode falls

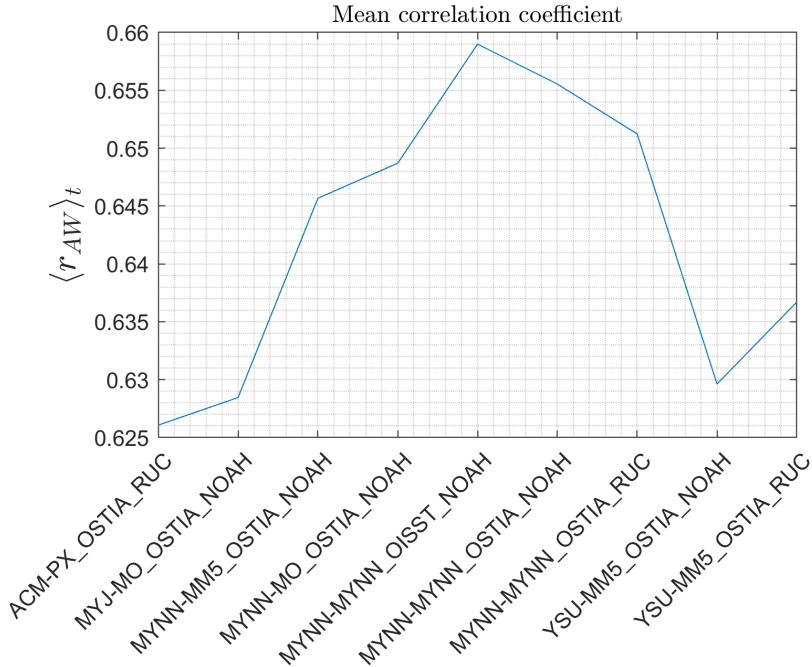


Figure 3.6: Mean Pearson’s correlation coefficient for each ensemble member.

close to 1 and that the distribution is negatively skewed. All ensemble members will show this behaviour. From figure 3.6 all ensemble members show a mean correlation coefficient between 0.62 and 0.66. These results confirm that phase shift are present for all ensemble members, therefore we continue our analysis by computing the WRF error metrics when conditioning on the correlation coefficient. The idea is to observe a reduction in error metrics when excluding less correlated data. Figure 3.7 shows different distributions of RE when conditioned on different thresholds of correlation coefficient. The distributions show similar mean values but different standard deviation. Figure 3.8 shows the distributions of TAE when conditioned on correlation coefficient. The mean is identical to figure 3.7 while the standard deviation doesn’t show the same reduction.

The resulting means and standard deviations of the distributions of RE for each ensemble member are compared in figures 3.9 and 3.10. Figures 3.11 and 3.12 show the same information as in figures 3.9 and 3.10 respectively, but data from different ensemble members are separated. From these figures we can see that removing lesser correlated snapshots will generally bring this mean RE to be more negative. This contradicts the initial idea that we’ll observe a reduction in error metric.

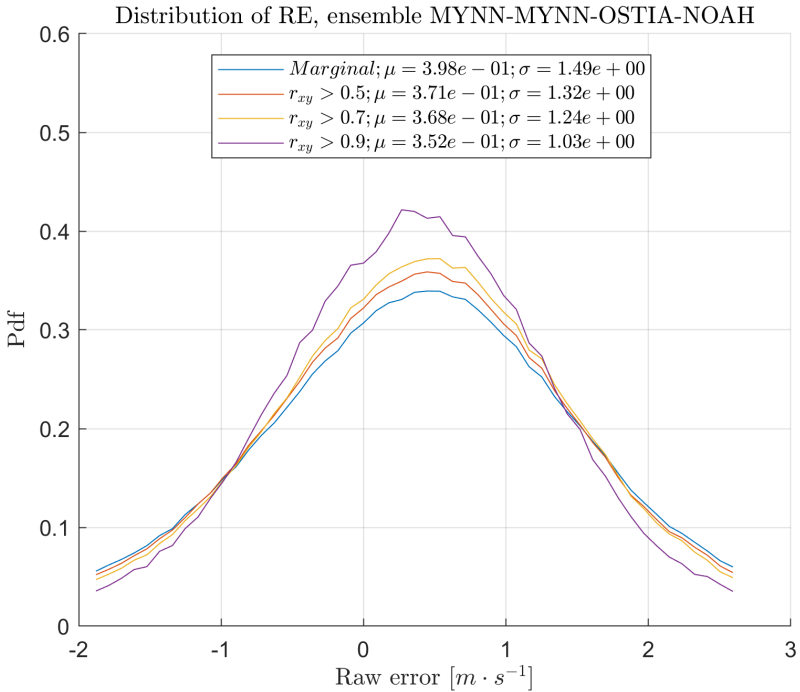


Figure 3.7: Distributions of raw error conditioned on correlation coefficient for the ensemble member MYNN-MYNN-OSTIA-NOAH. The legend states the threshold for the correlation coefficient and the mean and standard deviation for the distributions. Note that the standard deviation is decreasing when excluding less correlated data.

A possible explanation resides in noticing how the correlation coefficient is computed in equation 3.3. Since the correlation coefficient doesn't take into account the difference in mean value for the two signals, we wouldn't expect to necessarily decrease mean RE.

Instead, we would expect to decrease the RE standard deviation as a consequence of the removal of the highest deviations from the means. This is shown in figure 3.10 and 3.12. Given the results in this section, the raw error will not be analyzed when conditioning over wind speed, inverse Obukhov length or wind direction. The time averaged error will always be analyzed instead. We'll justify this choice by remembering the following. Firstly the mean RE and TAE coincide and secondly it is not necessarily true that improving the RE will also improve the TAE, as shown by the standard deviation of the error metrics in figures 3.7 and 3.8. The latter result reinforces the idea that if we use the WRF

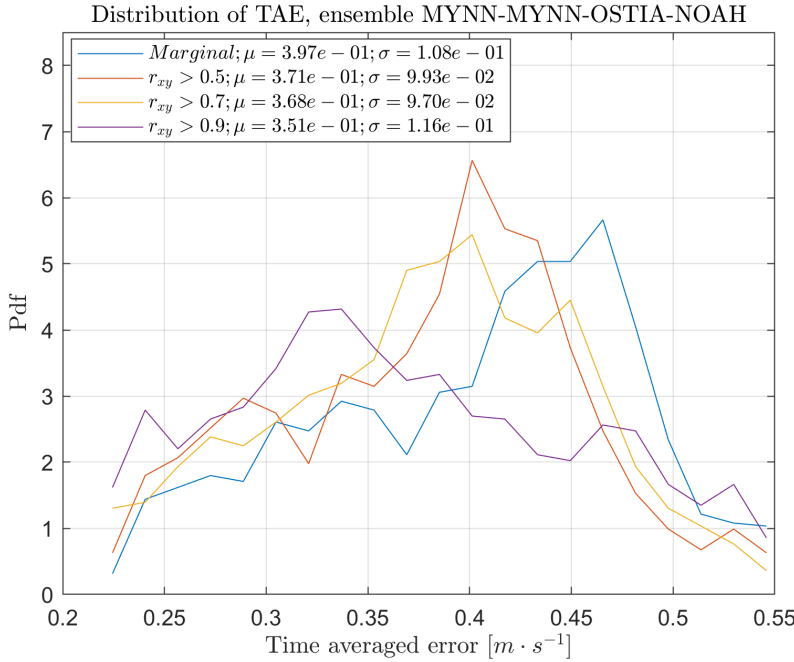


Figure 3.8: Distributions of time averaged error conditioned on correlation coefficient for the ensemble member MYNN-MYNN-OSTIA-NOAH. The legend states the threshold for the correlation coefficient and the mean and standard deviation for the distributions. Note that the standard deviation is not decreasing when excluding less correlated data.

data to compute any quantity such as the mean annual wind speed or the parameters of a Weibull distribution, we'll need a new error metric and a new analysis. Since the TAE is of practical use by evaluating the errors of a value that characterizes a wind climate, only this error metric is analyzed thought the whole thesis.

Given the results shown we can conclude that conditioning over spatial correlation has a significant impact on the standard deviation of RE (figures 3.7, 3.10 and 3.12) but not on the standard deviation of TAE (figure 3.8). The mean RE and mean TAE are also affected, but the differences don't necessarily reflect an improvement (figures 3.9 and 3.11). This difference is also not supported by a theoretical analysis of the definition of the coefficient (equation 3.3).

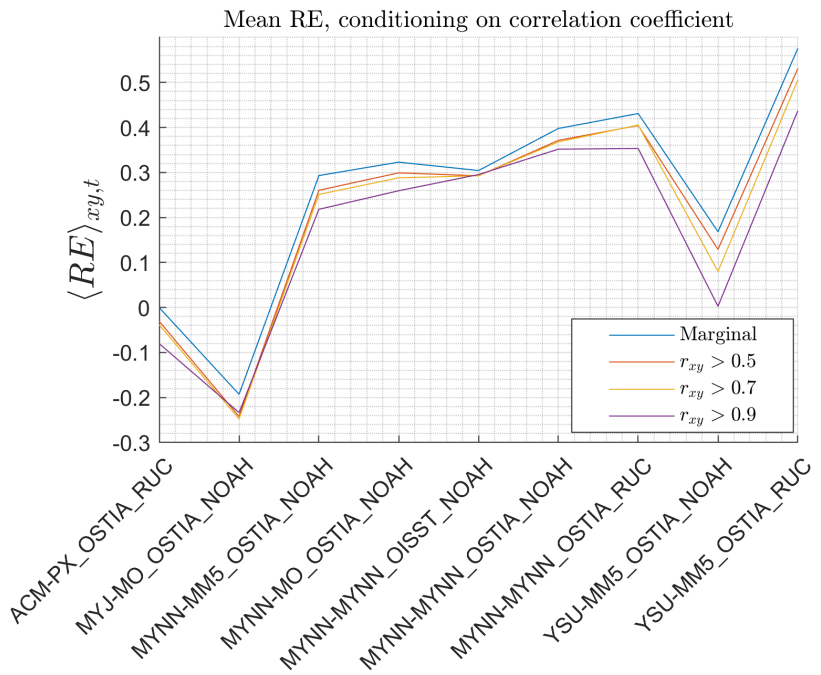


Figure 3.9: Mean raw error conditioned on correlation coefficient. The lines group the values for each condition, the latter being shown in the legend.

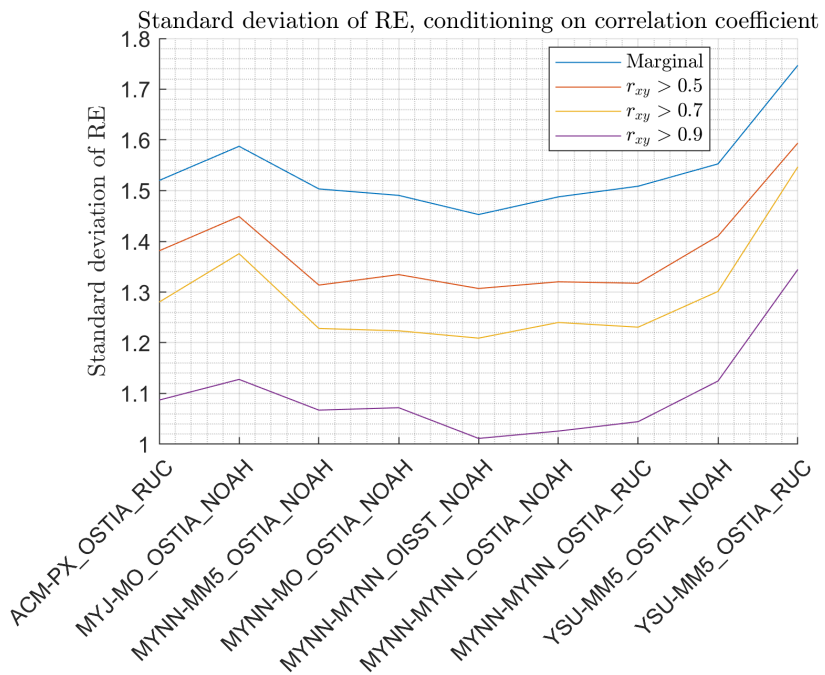


Figure 3.10: Standard deviation of raw error conditioned on correlation coefficient. The lines group the values for each condition, the latter being shown in the legend. The standard deviation is computed over all grid points and over all times.

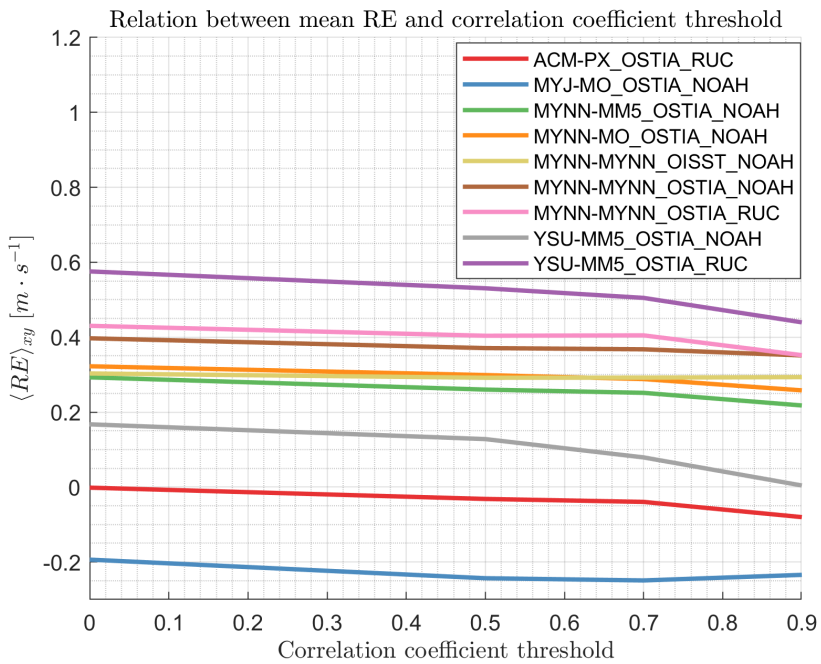


Figure 3.11: Mean raw error conditioned on correlation coefficient. The lines group the values for each ensemble member to show the relation between mean raw error and correlation coefficient threshold.

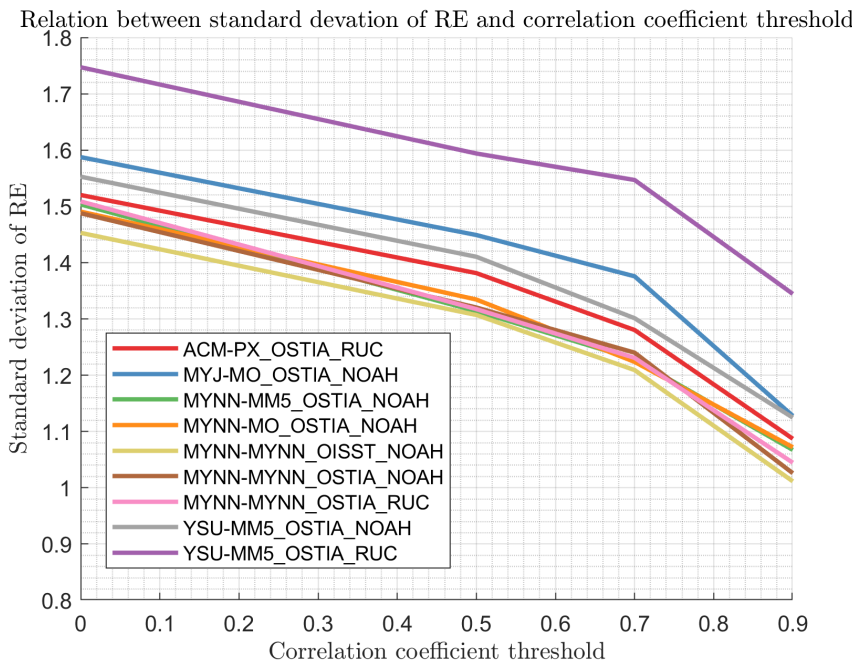


Figure 3.12: Standard deviation of raw error conditioned on correlation coefficient. The lines group the values for each ensemble member to show the relation between standard deviation of raw error and correlation coefficient threshold. The standard deviation is computed over all grid points and over all times.

3.2.3 Conditioning over wind speed

The conditioning on WRF wind speed follows a splicing dictated by a typical power curve of a wind turbine. Mainly we assume a cut-in wind speed of 4 m/s , nominal wind speed at 11 m/s and cut-out wind speed at 25 m/s . The splicing is concentrated below nominal wind speed. Wind speeds above nominal are considered as a single set of conditions. Due to the unknown uncertainty on WRF wind speed the nominal and cut-out wind speed have been transposed by $+1 \text{ m/s}$.

Figure 3.13 shows the mean TAE for the ensemble members. A clear pattern is visible, with mean TAE being more negative when conditioning on lower wind speeds. Knowing that lower wind speeds are observed more frequently with unstable conditions (p. 81-83, Berg et al., 2017), this point toward more negative mean TAE in unstable conditions than with stable conditions. Figure 3.14 shows the dependence of mean TAE with wind speed.

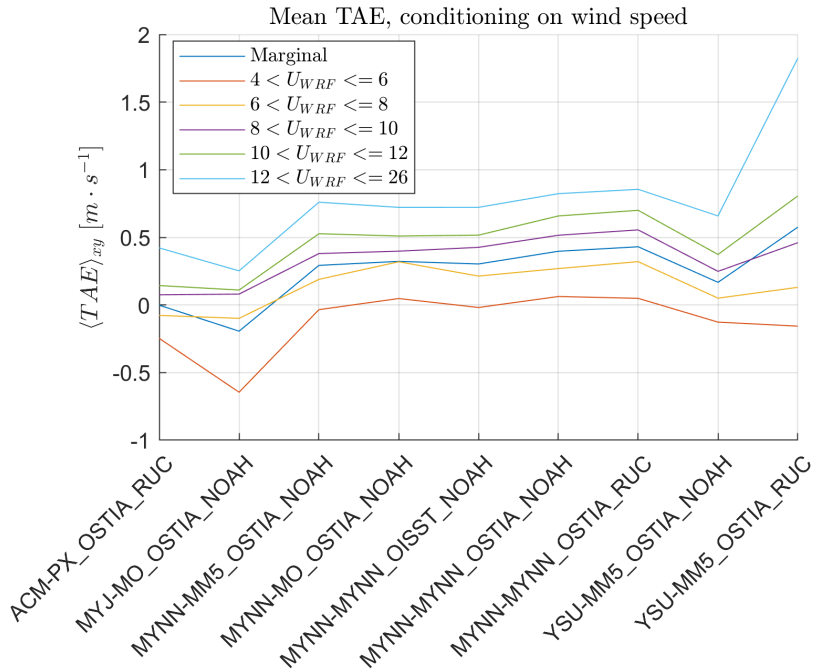


Figure 3.13: Mean TAE conditioned on wind speed for each ensemble member. The conditional variable U_{WRF} refers to the wind speed from the WRF data, different for each ensemble member. The lines divide the results per sets of conditions, the latter shown in the legend.

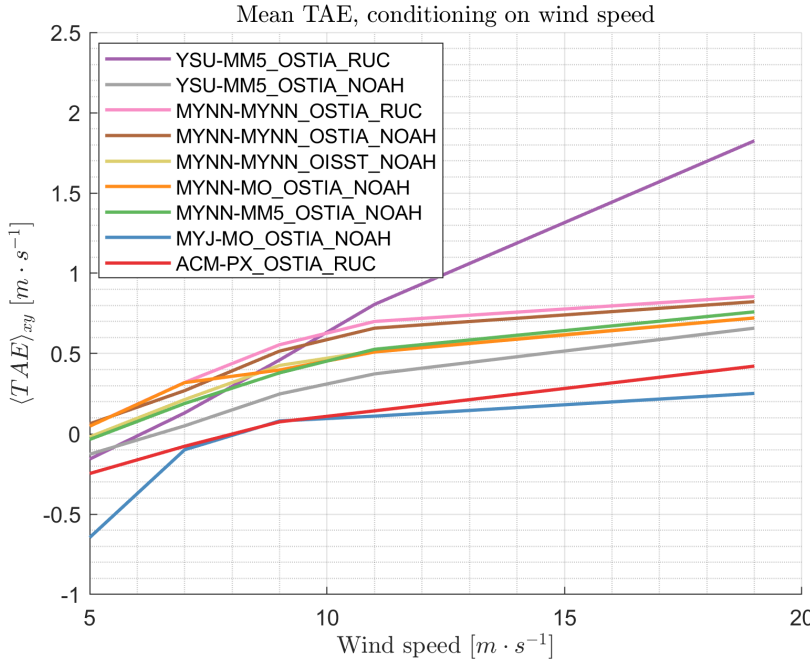


Figure 3.14: Mean TAE conditioned on wind speed for each ensemble member. The conditional variable is wind speed from the WRF data. The lines divide the results per ensemble member, the ensemble members name are shown in the legend.

Given that we observe that the mean TAE shows a semi-linear dependence on wind speed, it is useful to analyze this error metric when normalizing on wind speed. Figure 3.15 shows the mean normalized TAE for each ensemble member. We define the quantity in figure 3.15 as follows.

$$NTAE|_{x,y} \equiv \frac{TAE}{\langle U_a \rangle_t} \Big|_{x,y} \quad (3.4)$$

Where $\langle U_a \rangle_t$ refers to the mean wind speed for ASCAT data for a given grid point. All ensemble members shows that the normalized mean TAE doesn't increase past $11 [m \cdot s^{-1}]$ with exception for the ensemble members ACM-PX-OSTIA-RUC and YSU-MM5-OSTIA-RUC. The relative steepness of this normalized error metric at low wind speeds suggests that it is mostly affected by unstable conditions.

Figure 3.16 shows the mean NTAE weighted over the WRF wind speed frequency of occurrence. N_{COND} refers to the number of observations of WRF

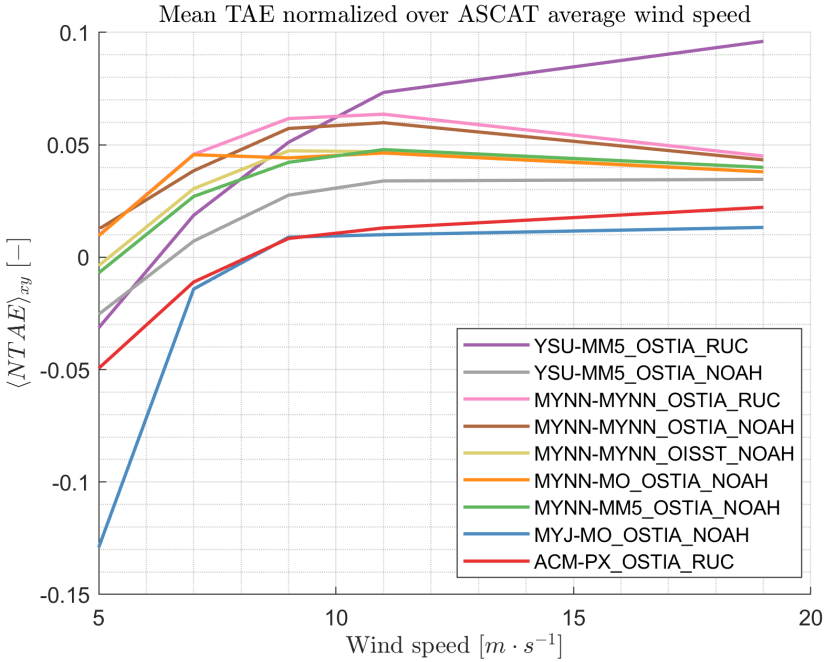


Figure 3.15: Mean TAE normalized by the time averaged wind speed for the ASCAT data. For each grid point the respective TAE has been divided by the corresponding average wind speed for the ASCAT data.

wind speed for each condition described in the legend. N_{TOT} refers to the total number of observations of WRF wind speed. From this figure we can observe the relative weight of each condition over the NTAE.

From figure 3.16 we can see that ensemble member MYJ-MO-OSTIA-NOAH presents the biggest influence over NTAE for lower wind speeds, pointing toward some discrepancies with the ASCAT data while computing over unstable atmospheric conditions. This behaviour is not observed when compared with the ensemble member YSU-MM5-OSTIA-NOAH, meaning that the problem can be linked with the PBL scheme MYJ but not with the surface layer scheme MO given the similarities between MYNN-MO-OSTIA-NOAH and MYNN-MM5-OSTIA-NOAH. The ensemble member YSU-MM5-OSTIA-RUC presents the same problem for the highest wind speeds. A comparison with the ensemble members YSU-MM5-OSTIA-NOAH restricts the problem to the land surface scheme RUC. When compared with the ensemble member MYNN-MYNN-OSTIA-RUC the land surface scheme RUC doesn't cause the same problem.

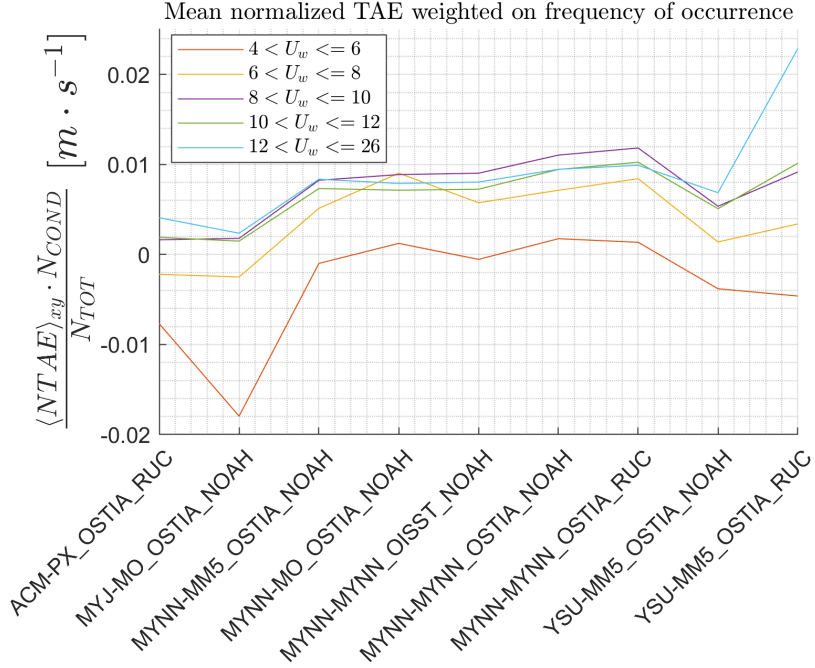


Figure 3.16: The mean normalized TAE has been weighted on frequency of occurrence for each condition. From the figure we can compare the relative effects of each condition over the marginal mean NTAE.

Figure 3.17 shows the standard deviation of TAE when conditioning over WRF wind speeds. The values are limited between $0.1 [m \cdot s^{-1}]$ and $0.21 [m \cdot s^{-1}]$, smaller than the related means of TAE shown in figure 3.13. The standard deviation of TAE decreases with WRF wind speed and shows the lower standard deviation for the marginal statistics. Comparing the ensemble members MYNN-MYNN-OSTIA-NOAH and MYNN-MYNN-OISST-NOAH, the OISST product causes an increase in standard deviation of TAE for marginal statistics and wind speeds $U_w \leq 8$.

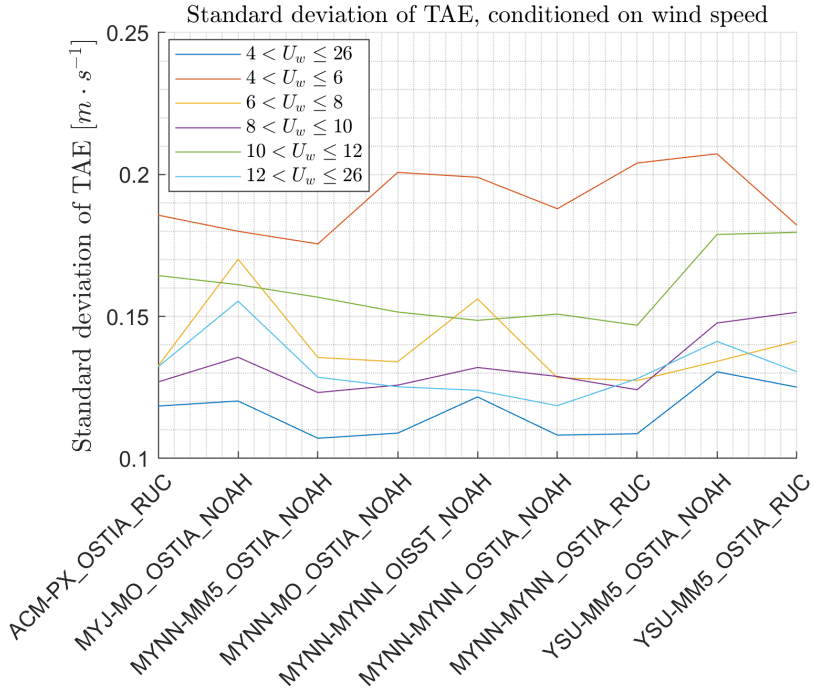


Figure 3.17: Standard deviation of TAE conditioned on WRF wind speeds, showing negative correlation with WRF wind speeds. The standard deviation is computed over all grid points.

3.2.4 Conditioning over inverse Obukhov length

From the results shown in the previous section differences in error metrics were observed for different WRF wind speeds. Knowing the relation between atmospheric conditions and wind speed (p. 81-83, Berg et al., 2017), we would expect to observe differences in error metrics when conditioning over the inverse Obukhov length as well. The conditions have been defined following the guidelines from the course *micrometeorology for wind energy* and the limits of $0.05 < 1/L \leq 0.0025$, $0.0025 < 1/L \leq -0.0025$ and $-0.0025 < 1/L \leq -0.05$ describe the conditions for stable, neutral and unstable conditions respectively. Atmospheric conditions outside these limits will be referred to as very stable and very unstable. Since the ASCAT data assumes neutral stability conditions (p. 39, EUMETSAT, 2015), we expect to observe a similar pattern to figure 3.13, with lower $\langle TAE \rangle_{xy}$ for unstable conditions (where ASCAT overestimates) and higher $\langle TAE \rangle_{xy}$ for stable conditions (where ASCAT underestimates). Figure

3.18 shows the mean TAE for the ensemble members when conditioned on $1/L$. Analyzing the results for neutral conditions (purple line in figure 3.18) it is clear

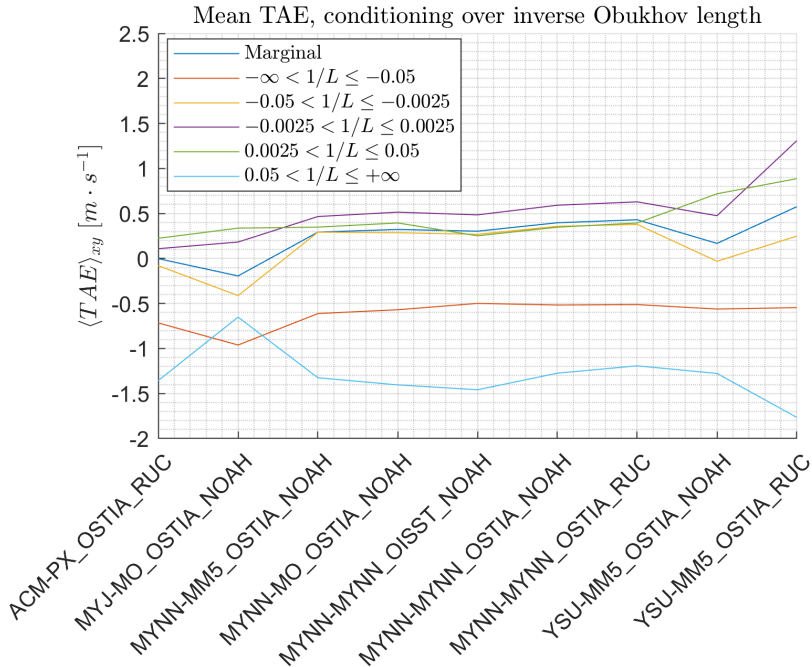


Figure 3.18: Mean TAE conditioned on $1/L$ for each ensemble member. Each line represents a condition with the blue line representing the marginal statistics. Very stable and unstable conditions show the worst mean TAE, while for neutral condition the mean TAE shows that most ensemble members overestimate the ASCAT data.

that the PBL scheme MYNN overestimate the wind speeds when compared to the ASCAT data. This result is derived from the formulation of TAE (equation 3.2b) and knowing that the wind speeds from the ASCAT data assumes neutral atmospheric conditions.

The mean TAE for very stable conditions (cyan line in figure 3.18) shows that the WRF simulations greatly underestimate the wind speeds. We can explain this behaviour by saying that the WRF simulations retain some mixing in stable conditions. This will transfer more momentum vertically through the layer and will result in a lower wind speed. Also, the assumption of neutral conditions for the ASCAT data means that the measurements are already underestimated. That said we would expect the WRF predictions over very unstable conditions

to show less TAE, but we instead observe values between $-0.5[m \cdot s^{-1}]$ and $-1[m \cdot s^{-1}]$. Given the formulation of TAE (equation 3.2b) we are unsure if the differences we observe are due to WRF underestimating or the ASCAT data overestimating due to the assumption of neutral condition.

By looking at the stable and unstable conditions for ensemble members with PBL scheme MYNN, the assumption of neutral conditions for the ASCAT data seems to balance with the differences in WRF predictions.

Figure 3.19 shows the standard deviation of TAE conditioned on $1/L$. Very stable conditions present values greater than the means of TAE in figure 3.18.

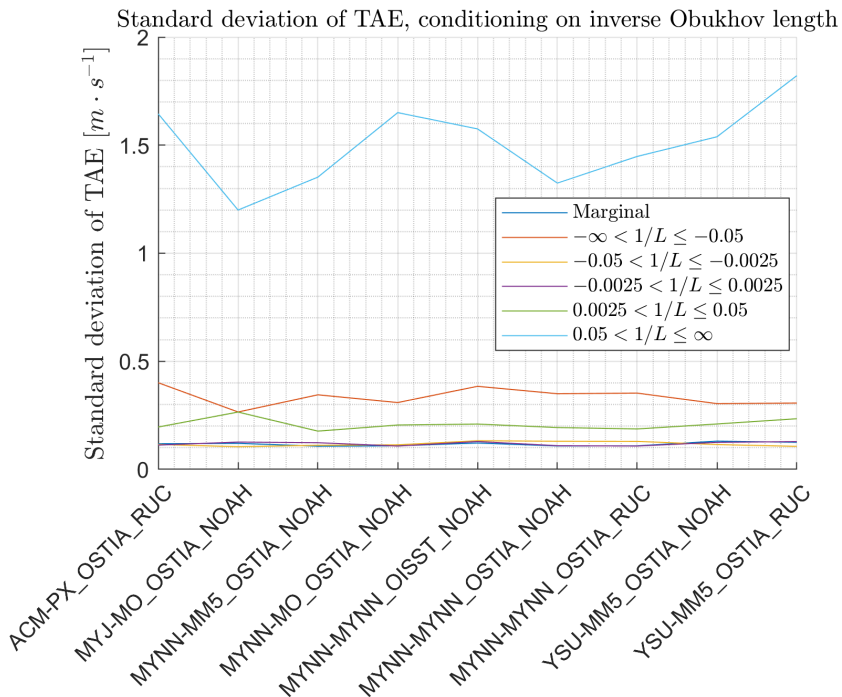


Figure 3.19: Standard deviation of TAE conditioned over $1/L$. Very stable conditions results in higher deviations from the mean. The standard deviation is computed over all grid points.

To understand the relative effect of each condition on the mean of marginal TAE we multiply by the frequency of occurrence of each condition.

Figure 3.20 shows the normalized TAE for each condition and ensemble member. Very stable conditions now result as having almost no influence over the mean marginal TAE. Instead all ensemble member show a higher influence for neutral conditions. Regarding the latter, the differences in ensemble members with the

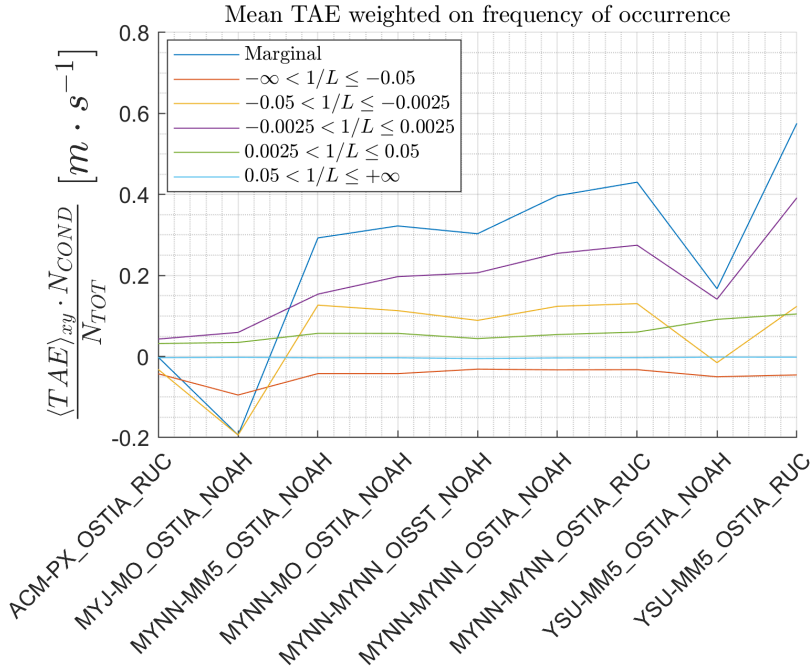


Figure 3.20: The mean TAE is multiplied by the frequency of occurrence of the corresponding condition. Very stable conditions shows no contribution to the marginal mean TAE while neutral conditions shows the highest contribution for almost all ensemble members.

PBL scheme MYNN are more evident than in figure 3.13. The only difference in these two figures is the frequency of occurrence of the conditions on $1/L$, meaning that, for example, the WRF simulations predicts neutral conditions more often for the MYNN-MYNN-OSTIA-RUC than MYNN-MM5-OSTIA-NOAH.

3.2.5 Conditioning over wind direction

Wind direction is not a variable on which we would expect to find any significant difference when conditioning our error metrics over it. Although not intended to bear any results, this analysis instead shown some interesting behaviours of the WRF simulations.

To ease the reading of the following figures, the conditions have been chosen to reflect the four cardinal directions. The North is located at 0° and East at 90° .

Figure 3.21 shows the mean TAE conditioned over WRF wind direction.

From easterly directions we observe a significant difference in mean TAE for

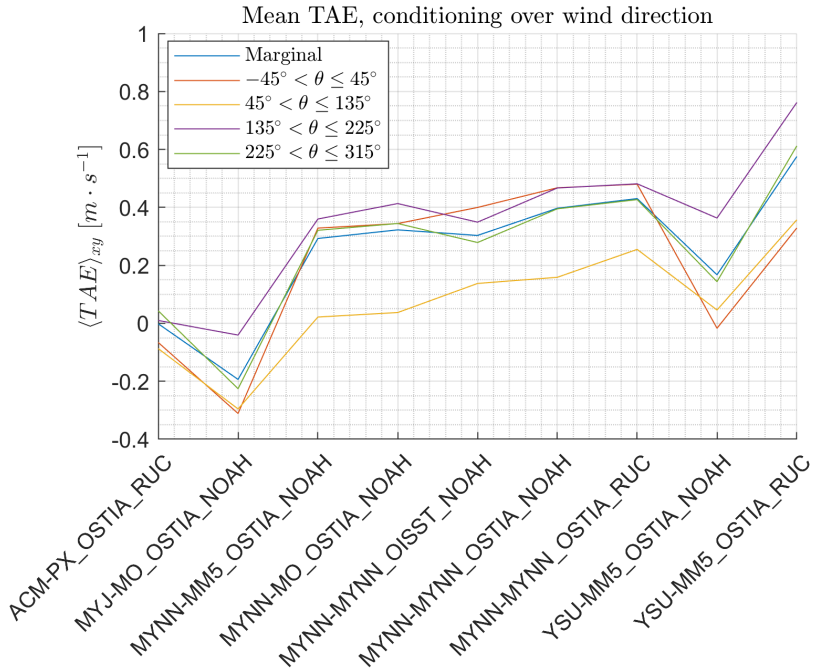


Figure 3.21: Mean TAE conditioned on WRF wind direction. Easterly directions show a significantly different mean TAE for ensemble members with PBL scheme MYNN.

all ensemble member with PBL scheme MYNN. The reason could be related to why the wind blows from east in the North sea region. The wind comes from east in the rare but persistent occasions for which high pressure system is located above Denmark. In this case a WRF spatial phase shift could explain the differences. A second explanation could be found by observing that it is possible that different wind directions will give rise to different wind speeds, and therefore different mean TAE by the relation between TAE and WRF wind speed as shown in figures 3.13 and 3.14. To contextualize the second explanation we show the mean wind speed for each wind direction condition and each ensemble member. This result is visible in figure 3.22. From figure 3.22 we can see how the mean WRF wind speed changes with direction. It is not true that higher mean wind speeds will result in higher mean TAE, although this result can be observed for single conditions. The latter argument also points toward a significant difference between the directions other than wind speed. A

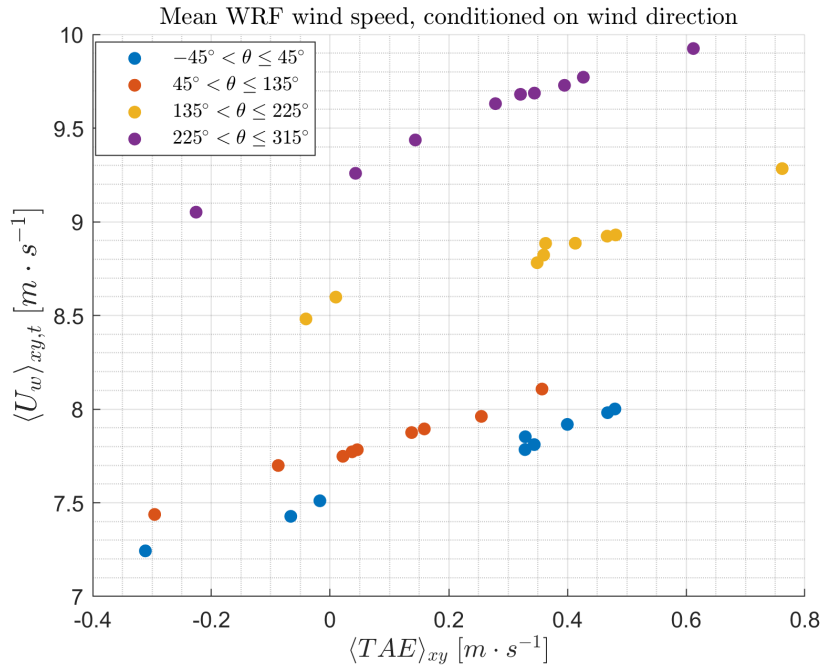


Figure 3.22: Mean WRF wind speed conditioned on WRF wind direction as a function of mean TAE. The figure shows a clear relation between mean WRF wind speed and mean TAE when conditioned on wind direction.

third explanation could be made observing that winds from easterly directions are the closest to land (Denmark, Norway). If that would be the case, a study of the TAE conditioned on both direction and spatial location will reveal the differences.

To this end we divide the area of interest shown in figure 2.5 in a East area and a West area. The whole area of interest will be called full area. The East area covers a quarter of the full area, while the West are the remaining three quarters. Figure 3.23 shows the partitioning of the area, with the yellow area representing the East area and green representing the West area. Conditioning on these areas and on wind direction we can isolate the spatial effects for easterly winds. Figure 3.24 shows the mean TAE computed on the full, East or West area for all directions (marginal) or the east direction only. In figure 3.24 almost all ensemble members show a further reduction in mean TAE with exception of MYJ-MO-OSTIA-NOAH, MYNN-MYNN-OSTIA-RUC and YSU-MM5-OSTIA-RUC.

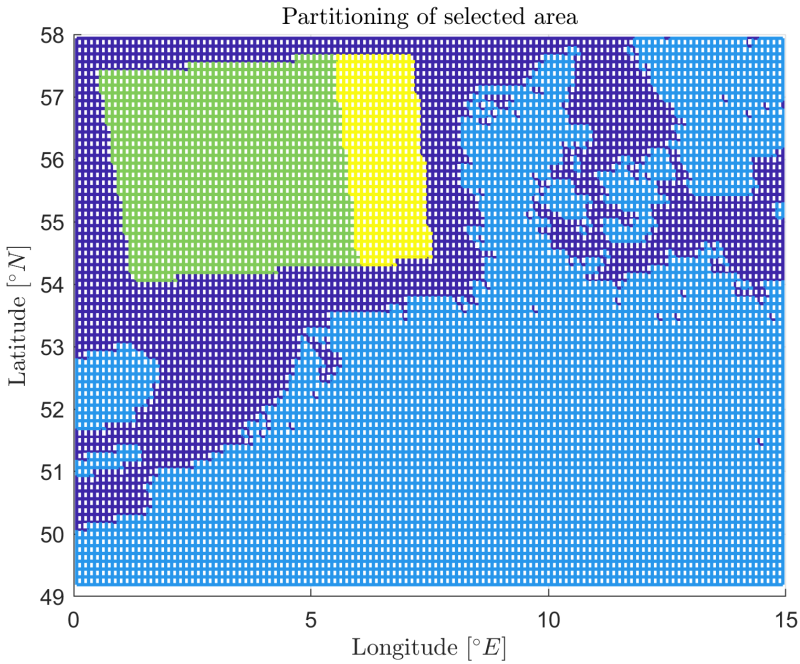


Figure 3.23: The selected area of interest in figure 2.5 has been divided into two smaller areas, of which one (yellow) is facing East to study the relation between distance from coast and mean TAE for easterly winds.

This could show inconsistency with the reasoning, and one can show that the presence of land should not interfere with the development of the surface boundary layer (Troen and Petersen, 1989).

Ultimately we'll analyze the standard deviation of TAE, shown in figure 3.25. This figure shows a similar behaviour for most ensemble members with the highest values for easterly winds and lowest for winds from the West. The land surface scheme RUC seems appears correlated with higher standard deviations for northern winds. This can be checked by comparing the ensemble members MYNN-MYNN-OSTIA-RUC with MYNN-MYNN-OSTIA-NOAH, and YSU-MM5-OSTIA-RUC with YSU-MM5-OSTIA-NOAH.

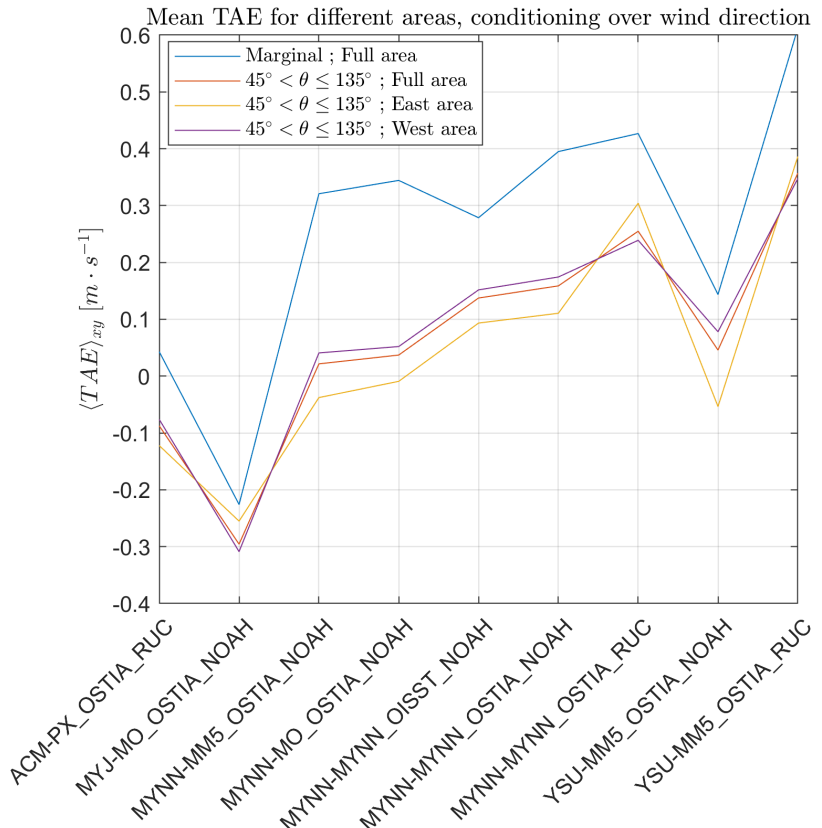


Figure 3.24: Mean TAE when conditioned on east direction and areas as shown in figure 3.23. Most ensemble members present a further reduction of mean TAE when conditioning on the East area.

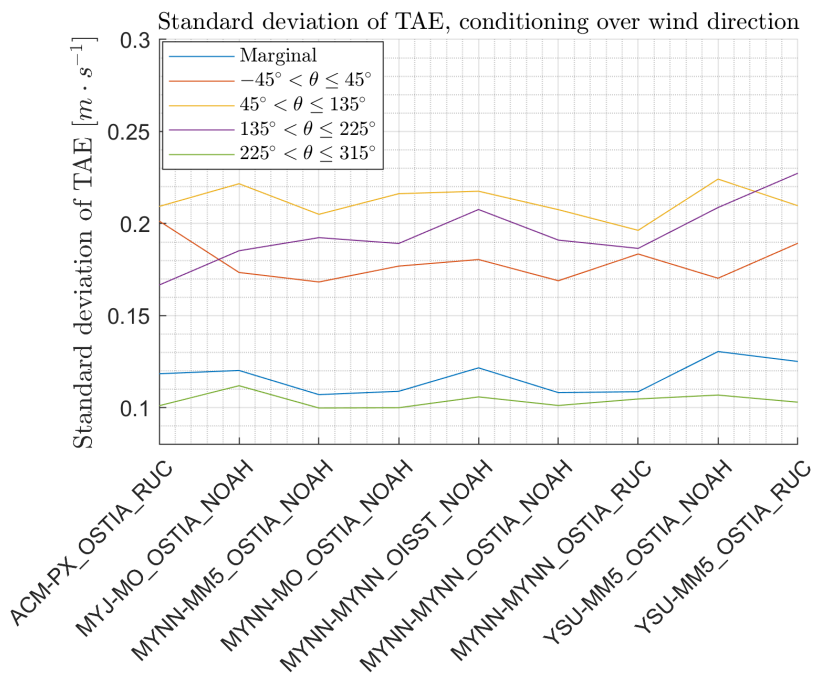


Figure 3.25: Standard deviation of TAE when conditioned on WRF wind direction. The ensemble members show a similar behaviour. The standard deviation is computed over all grid points.

3.3 Correction of ASCAT data

When presenting the ASCAT wind speeds we've also noted that these data are obtained assuming neutral wind conditions. This assumption limits our understanding of the error metrics, especially when conditioning on stability. The neutral logarithmic wind profile can be written as:

$$u(z) = \frac{u_*}{k} \log\left(\frac{z}{z_0}\right) \quad (3.5)$$

Where $u(z)$ is the wind speed, u_* represent friction velocity (from the WRF simulations), z measures height from the surface, z_0 is the surface roughness length and k is the Von Kármán constant $k \approx 0.4$.

Following the Monin-Obukhov similarity theory, to include stability effects a stability correction function $\Psi_m\left(\frac{z}{L}\right)$ is added to the neutral logarithmic law:

$$u(z) = \frac{u_*}{k} \left[\log\left(\frac{z}{z_0}\right) + \Psi_m\left(\frac{z}{L}\right) \right] \quad (3.6)$$

By reworking the equations 3.5 and 3.6 we get the formulation for the stability correction as:

$$U_{A, \text{corrected}} = U_A - \frac{u_*}{k} * \Psi_m\left(\frac{z}{L}\right) \quad (3.7)$$

Several corrections have been proposed to take into consideration stability effects (Holtslag et al., 2014). We'll use the formulations: (Beljaars and Holtslag, 1991) For unstable conditions:

$$\begin{aligned} -0.1 &< \frac{1}{L} \leq 0 \\ \Psi_m\left(\frac{z}{L}\right) &= 2 * \log\left(\frac{1+x}{2}\right) + \log\left(\frac{1+x^2}{2}\right) - 2 * \arctan(x) + \pi/2 \end{aligned} \quad (3.8a)$$

$$x = \left(1 - \gamma * \frac{z}{L}\right)^{1/4} \quad (3.8b)$$

With $\gamma = 16$. For stable conditions:

$$\Psi_m\left(\frac{z}{L}\right) = -\beta\left(\frac{z}{L}\right) \quad ; \quad 0 < \frac{1}{L} < 0.1 \quad (3.9)$$

With $\beta = 4.7$.

This correction is based on values of $1/L$ from the WRF simulations, while the height from the surface is $z = 10m$. The surface roughness length z_0 is computed using the following formulation (p. 77, Berg et al., 2017).

$$z_0 = Ac \frac{u_*^2}{g} \quad (3.10)$$

Where the dimensionless Charnock constant $Ac = 0.0162$, u_* is the friction velocity (from WRF simulations) and g is the acceleration of gravity $g = 9.81 [m \cdot s^{-2}]$. Since the correction is based on variables from the ensemble members, we'll obtain a different correction for the ASCAT data for each ensemble member. An example of distribution of correction is given if figure 3.26, where the quantity $-\frac{u_*}{k} * \Psi_m\left(\frac{z}{L}\right)$ is shown to reflect the formulation in equation 3.7.

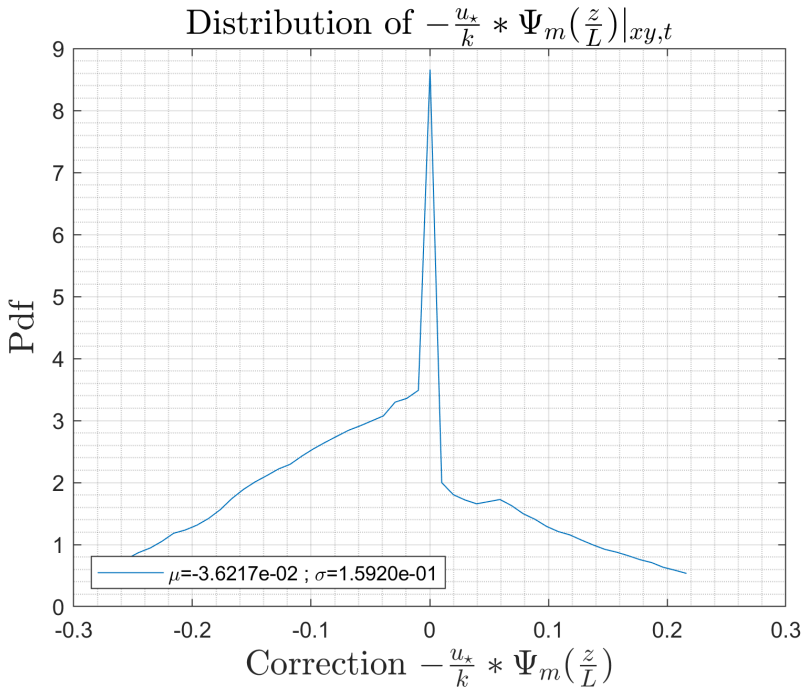


Figure 3.26: Distribution of the stability correction $-\frac{u_*}{k} * \Psi_m\left(\frac{z}{L}\right)$ as shown in equation 3.6 for the ASCAT data. The legend shows mean and standard deviation.

The distribution in figure 3.26 shows a peak over neutral conditions, where the correction approaches zero. The distribution also shows a higher density for negative values in accordance with the higher density for unstable conditions in figure 3.4.

With the stability corrected ASCAT data we can repeat our analysis of the error metrics for the WRF data against the corrected ASCAT data.

Figure 3.27 shows the mean $-\frac{u_*}{k} * \Psi_m\left(\frac{z}{L}\right)$ conditioned on inverse Obukhov

length. From this figure the correction can be understood as a function of $1/L$. We observe that the correction doesn't affect neutral winds, instead increases neutral wind speeds in stable conditions and decreases neutral wind speeds in unstable conditions. The first condition $-0.1 < 1/L \leq 0.1$ can be interpreted as marginal since the values of ASCAT data associated with values of $1/L$ outside these limits are discarded.

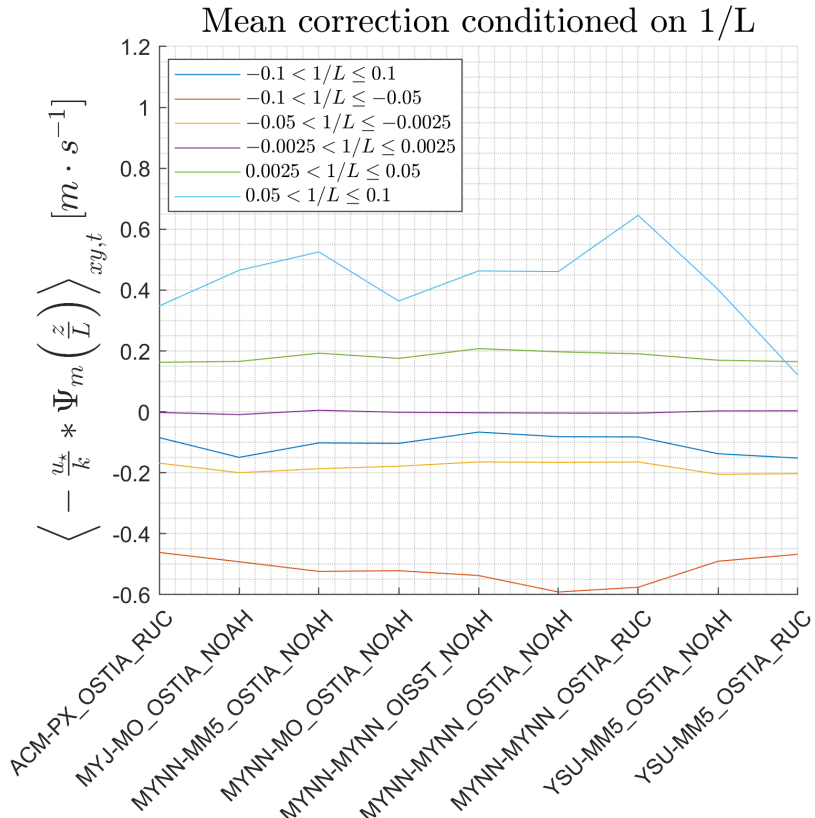


Figure 3.27: Mean stability correction conditioned on $1/L$. Neutral winds are unaffected by the correction (purple line) while very stable and very unstable conditions (cyan and red lines) show the highest and lowest mean correction respectively.

Figure 3.28 shows the mean $-\frac{u_*}{k} * \Psi_m \left(\frac{z}{L} \right)$ conditioned on WRF wind speed. From this figure we can observe that the correction is negative for all wind speed conditions, but relatively smaller than in figure 3.27 (all the conditioned values are contained between the blue and purple line shown in figure 3.27). A

distinct pattern is present, with lower wind speeds showing lower values for the correction.

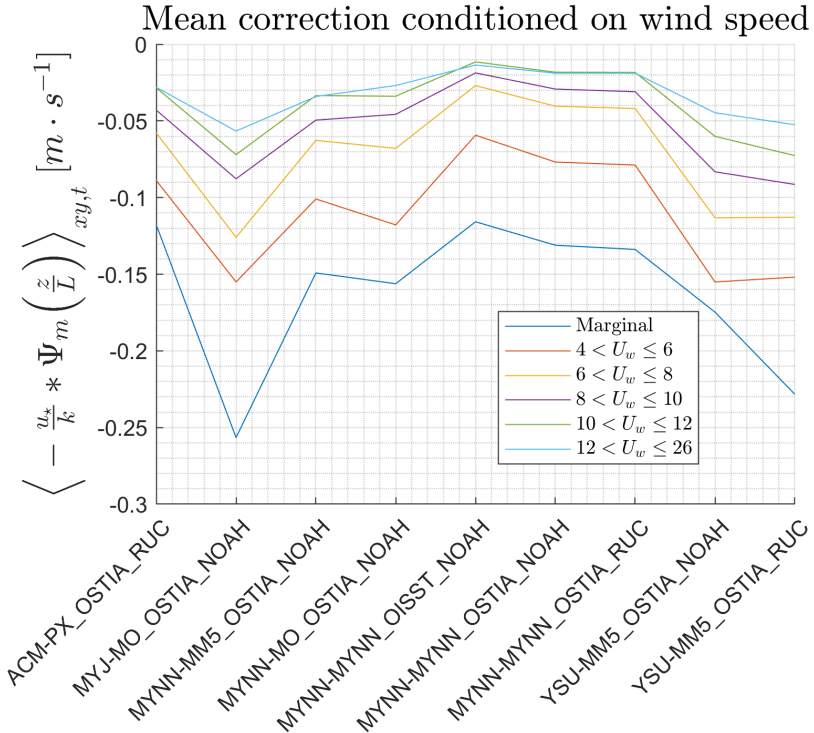


Figure 3.28: Mean stability correction conditioned on WRF wind speed. The mean correction increases with WRF wind speed for all ensemble members.

Figure 3.29 shows the mean $-\frac{u_*}{k} * \Psi_m\left(\frac{z}{L}\right)$ conditioned on WRF wind speed. The results for the correction conditioned on wind direction are not to be compared with those obtained for mean TAE, since this result is based only on values of $1/L$. Instead, it doesn't look like the easterly winds are affected in a different way than the other directions.

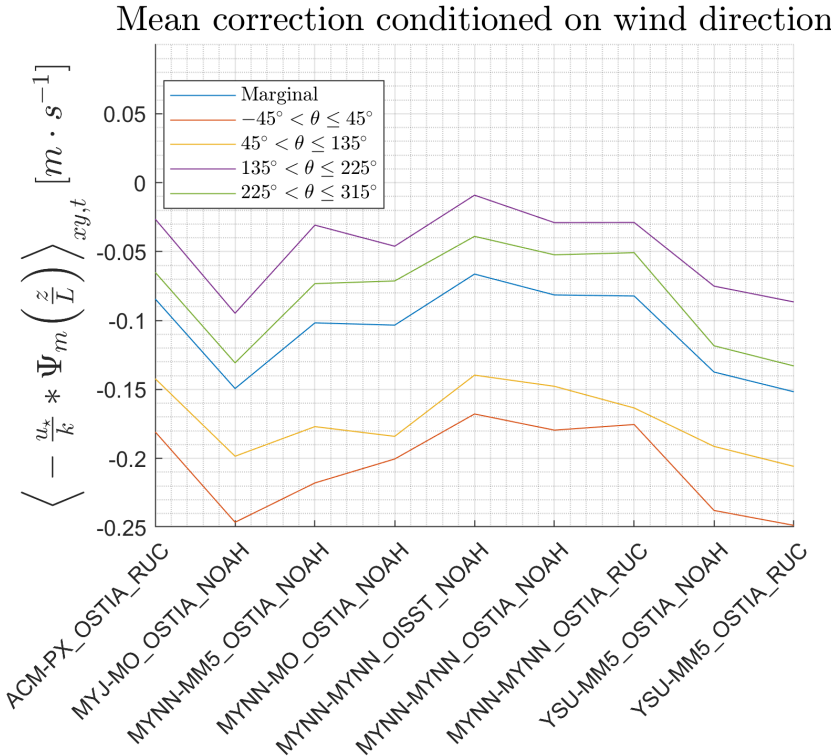


Figure 3.29: Mean stability correction conditioned on WRF wind direction. A pattern is clearly visible, with mean stability correction showing a dependence on WRF wind direction.

3.4 Conditional statistics with stability corrected ASCAT data

We are now going to repeat the same procedure to obtain the conditional statistics for the error metrics as previous sections, but with corrected ASCAT data. Figure 3.30 shows the mean TAE when conditioning over WRF wind speed and comparing against the corrected ASCAT data. The values in this figure look very similar with those obtained without the corrected ASCAT data (figure 3.13). This is since the values for the correction in figure 3.28 are relatively small in comparison.

Given this result in figure 3.30, WRF for all configurations considered, overes-

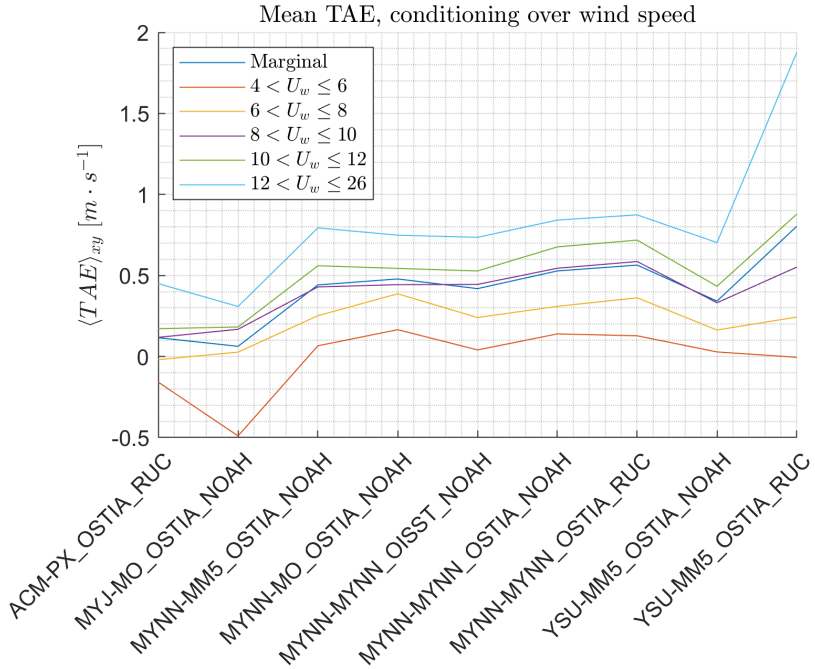


Figure 3.30: Mean TAE conditioned on WRF wind speed and computed with corrected ASCAT data. The WRF simulations are shown to overestimate the ASCAT data on almost all conditions.

timates the mean winds over $6 [m \cdot s^{-1}]$ compared to ASCAT. Figure 3.30 also shows that ensemble variability is mostly due to PBL scheme. Figure 3.31 shows the mean TAE conditioned on $1/L$ and computed with the corrected ASCAT data. Compared with figure 3.18 we observe a significant improvement for very unstable conditions for all ensemble members. Looking at figure 3.27 the mean TAE for this condition increases (due to the negative sign in equation 3.2b). This increase in mean TAE is also present for unstable conditions, but doesn't reflect in an improvement over mean TAE (with exception for the ensemble member MYJ-MO-OSTIA-NOAH). A similar argument is valid for stable and very stable conditions, with mean TAE improving for all ensemble members over stable conditions but decreasing in performance for very stable conditions.

Figure 3.32 shows the mean TAE conditioned on wind direction and computed with the corrected ASCAT data. Northern winds show a significantly higher mean TAE when compared with the non corrected ASCAT data in figure 3.21. Easterly winds show an increase in mean TAE. These two directions are also

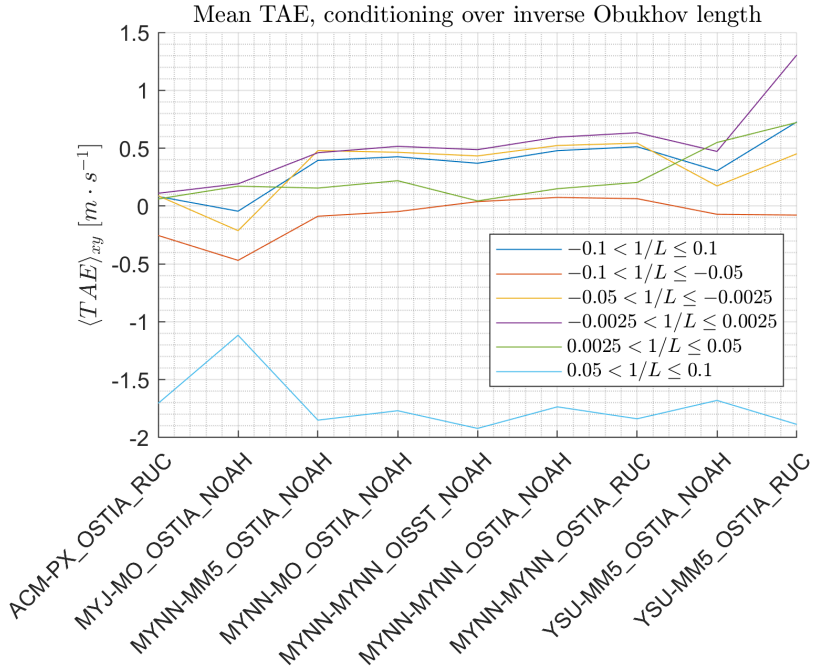


Figure 3.31: Mean TAE conditioned over $1/L$ and computed with corrected ASCAT data. The correction changed the relation between stability and mean TAE, with very unstable conditions showing the highest change.

the most affected by the correction as shown in figure 3.29.

The standard deviation of TAE is also found to change after the correction of ASCAT data, although the differences are small. The most meaningful difference is observed for the marginal standard deviations of TAE, shown in figure 3.33. The average difference in standard deviations is $0.015[m \cdot s^{-1}]$, or an average of 13% decrease compared to the uncorrected data.

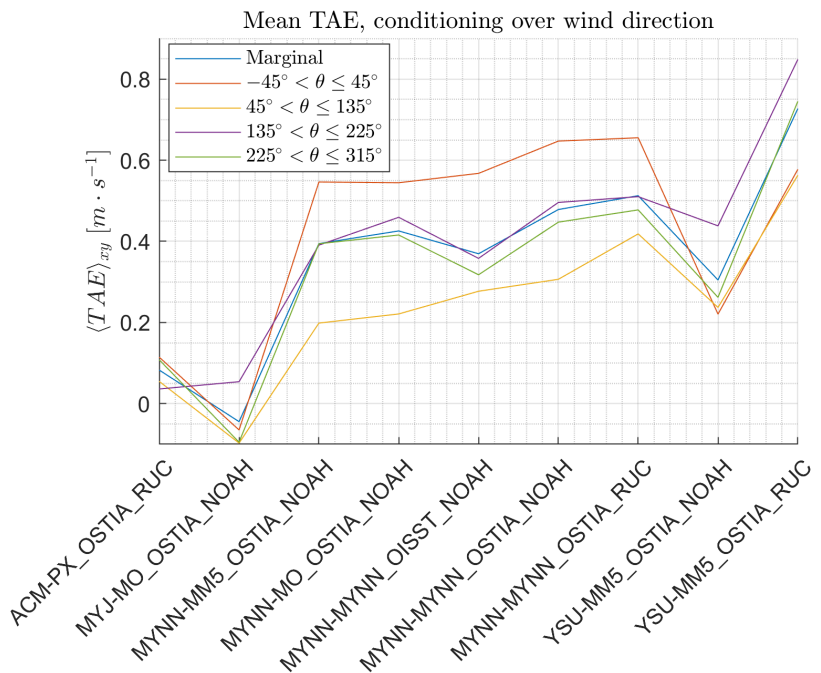


Figure 3.32: Mean TAE conditioned over WRF wind direction and computed with corrected ASCAT data. The correction improves the mean TAE for easterly winds and decreases its performance for northern winds.

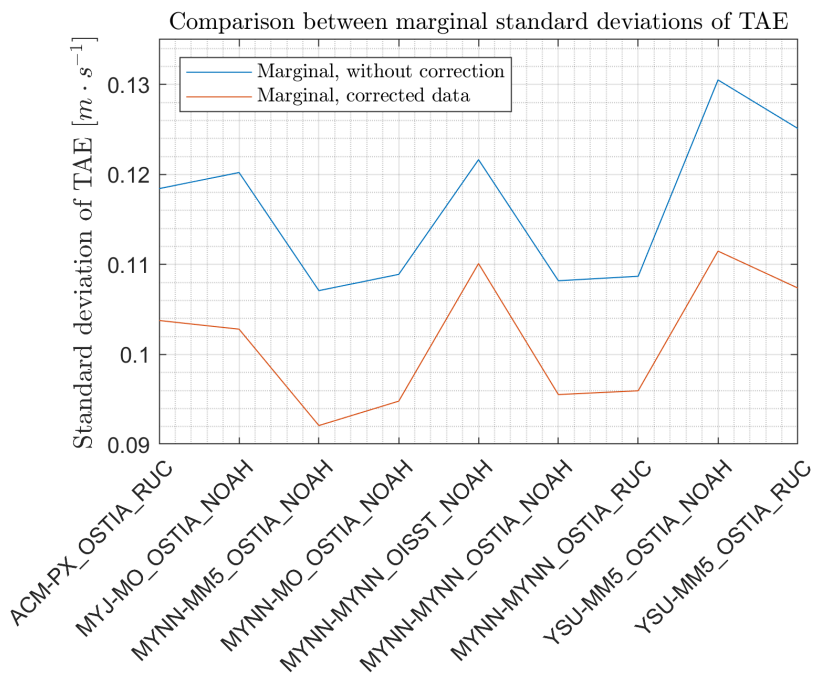


Figure 3.33: The marginal standard deviations of TAE are shown for each ensemble member prior and after correction of ASCAT data. The average difference in standard deviations is $0.015[m \cdot s^{-1}]$.

CHAPTER 4

Discussion

This thesis defined and analyzed different error metrics for 9 WRF ensemble members against ASCAT measurements, over a selected area of interest and using conditional statistics. Initially we defined an interpolation procedure. This was done with the definition of two interpolation error metrics and the comparison of the latter for the various choices for the interpolation (space and time grid, method). To study the WRF errors we defined and analyzed two error metrics. These error metrics are then conditioned over correlation (between WRF and ASCAT wind speed fields) and WRF wind speed, inverse Obukhov length and wind direction. A stability correction for the ASCAT data is presented and then the error metrics are analyzed again with the corrected ASCAT data.

The interpolation procedure was chosen based on consideration of possible choices of interpolation spatial and temporal grid, and interpolation method. To this end two interpolation error metrics are defined, with the difference in average (Δ_A , defined in equation 2.1) describing the overestimation or underestimation of the highest or lowest wind speeds and the ratio of variance (RVAR, defined in equation 2.2) measuring the overestimation or underestimation of both highest and lowest wind speeds.

The choice of interpolation grid is based on the results for the interpolation error metrics over the selected area of the North sea domain (figure 2.5). The two possible choices are to interpolate the ASCAT data onto the WRF grid or to interpolate the WRF data onto the ASCAT grid. The results show a higher standard deviation of Δ_A when interpolating the WRF data onto the ASCAT grid and similar means for Δ_A for both choices (figures 2.6 and 2.8). The study

over RVAR shows a higher mean RVAR when interpolating the WRF data onto the ASCAT grid, although both choices result in an underestimation of the highest and lowest wind speeds. The standard deviations for RVAR are very similar for both choices (figures 2.7 and 2.9). Therefore the interpolation error metrics indicate a slightly better performance when interpolating the ASCAT data onto the WRF grid.

The time interpolation offers again the choice of interpolating the ASCAT data onto the WRF time stamps or the WRF data onto the ASCAT time stamps. Since the ASCAT data offers a maximum of 4 measurements per day with the latter being scattered unevenly during the day, while the WRF data presents one data point per half hour (48 total per day) we prefer to interpolate the WRF data onto the ASCAT time stamps (p. 57-58, Li and Heap, 2008).

The choice of interpolation method is based on the data from the UK domain, selecting only grid points at least 6 km away from land. When comparing results from each interpolation method, the choices of **bilinear** and **bicubic** show very similar distributions for Δ_A and RVAR (figures 2.10, 2.11, 2.12 and 2.13). We'll therefore prefer the bilinear method due to lower computational time. Given the results for grid interpolation, time interpolation and interpolation method, we chose to interpolate the WRF data onto the ASCAT grid and time stamps using the bilinear method, leaving the ASCAT data untouched by the interpolation.

When defining the error metrics, we introduce the raw error (RE, equation 3.2a) as a metric to represent the correspondence between individual simulations and measurements and the time-averaged error (TAE, equation 3.2b) to represent the correspondence between average simulations and measurements.

The effects of WRF phase shift are represented by the (Pearson) correlation coefficient (equation 3.3) and the error metrics are analyzed when conditioning over this coefficient. The results for ensemble MYNN-MYNN-OSTIA-NOAH in figures 3.7 and 3.8 show that while the means for RE and TAE are identical, the standard deviations for their distributions differs. Specifically the $\sigma_{RE_{xy,t}}$ is always one order of magnitude higher than the mean ($\sigma_{RE_{xy,t}} > \langle RE \rangle_{xy,t}$), while the $\sigma_{TAE_{xy}}$ is always lower than its mean ($\sigma_{TAE_{xy}} < \langle TAE \rangle_{xy}$), with comparable order of magnitude. Further analysis for RE when conditioning on correlation coefficient is presented in figures 3.9 and 3.10, where we can observe again a higher $\sigma_{RE_{xy,t}}$ than $\langle RE \rangle_{xy,t}$ for all ensemble members. These first results shows a clear difference between the two error metrics, suggesting that the uncertainties must be derived (and are therefore applicable) with regard to a specific error metric. Figures 3.10 and 3.12 also show that the $\sigma_{RE_{xy,t}}$ lowers consistently when conditioning over higher thresholds for the correlation coefficient, while figure 3.11 shows that the relation between mean RE and correlation coefficient threshold is not as clear.

When conditioning TAE over WRF wind speed, we observe that its mean shows a positive correlation with WRF wind speed (figures 3.13 and 3.14). A physical interpretation of the phenomena suggests also a correlation between mean TAE and atmospheric stability, with lower mean TAE for unstable conditions and higher mean TAE for stable conditions. This interpretation is supported when conditioning over $1/L$ in figure 3.18 with exception for the ensemble members driven by the PBL scheme MYNN, that show no significant difference instead. Given the monotonic relation between TAE and WRF wind speed in figure 3.14, the TAE has been normalized over the mean ASCAT wind speed per grid point (NTAE, defined in equation 3.4) in figure 3.15. This shows a relative increase in TAE until $9 [m \cdot s^{-1}]$ followed by a relative decrease in TAE, for all ensemble members with exception of YSU-MM5-OSTIA-RUC and ACM-PX-OSTIA-RUC. Generally the NTAE results confined between -5% and $+5\%$. The NTAE has then been weighted on frequency of occurrence of the WRF wind speed in figure 3.16. From this result we can observe that lower wind speeds have a greater impact over the mean NTAE for the ensemble MYJ-MO-OSTIA-NOAH and this different result can be traced to the PBL scheme MYJ. The ensemble member YSU-MM5-OSTIA-RUC presents the same problem for higher wind speeds, and this result can be attributed to the surface scheme RUC.

A correspondence between WRF wind speed and $\sigma_{TAE_{xy}}$ is shown in figure 3.17, although not consistent for every ensemble member. Again the $\sigma_{TAE_{xy}}$ results smaller than $\langle TAE \rangle_{xy}$, but significant differences are noted for smaller WRF wind speeds when compared to the marginal counterpart.

The conditioning of TAE over inverse Obukhov length is performed to separate the effects of different stability conditions. The mean TAE shown in figure 3.18 shows a consistent overestimation of the ASCAT wind speeds for the ensemble members driven by the PBL scheme MYNN. For these ensemble members we also observe similar mean TAE for stable and unstable conditions. The mean TAE over very stable and very unstable conditions results in a underestimation of ASCAT wind speeds for all ensembles. The $\sigma_{TAE_{xy}}$ shows a value comparable with $\langle TAE \rangle_{xy}$ for very stable conditions, and generally half of $\langle TAE \rangle_{xy}$ for very unstable conditions. The $\sigma_{TAE_{xy}}$ is higher than its marginal value for stable conditions and comparable with its marginal value for neutral and unstable conditions. The results obtained for stable conditions could be explained with the tendency of WRF to overestimate the momentum transfer between layers when in stable conditions, while the result over very stable conditions could be explained by the assumption of neutral conditions for the ASCAT data. We can then generalize these results in terms of uncertainty, with lower uncertainty for the WRF mean annual wind speed over neutral and unstable conditions. In figure 3.20 we show the mean TAE weighted on frequency of occurrence for the stability classes. Very stable conditions don't present any influence over the marginal value, with neutral condition influencing the most for the ensemble

members driven by the PBL scheme MYNN and YSU.

The conditioning of TAE over WRF wind direction shows a unexpected result for Easterly winds in figure 3.21, while other directions show comparable results. This low value for mean TAE is analyzed in figure 3.24 and a further decrease of mean TAE is observed when conditioning over grid points closer to land for almost all ensemble members. The presence of land up-hill could explain this lower mean TAE, but this reasoning is shown to be inconsistent for all ensembles. The $\sigma_{TAE_{xy}}$ is found to be correlated to the WRF wind direction in figure 3.25, although this correlation is not clear for some ensemble members (ACM-PX-OSTIA-RUC and YSU-MM5-OSTIA-RUC). An ensemble to ensemble comparison shows that the surface scheme RUC is responsible for higher standard deviations of TAE for Northern winds. To interpret these results in terms of uncertainty, we argue that the higher uncertainty for WRF mean annual wind speed is presented for Easterly winds, with the surface scheme RUC introducing more uncertainty for Northern winds.

Following the results when conditioning over $1/L$, we implement a stability correction function for the ASCAT data in equations 3.8a and 3.9. This correction allows us to analyze the error metrics without the assumption of neutral stability for the ASCAT data. When conditioning TAE over WRF wind speed in figure 3.30, we can observe that the WRF simulations overestimate the corrected wind speeds for almost all wind speed ranges. The conditioning over $1/L$ in figure 3.31 shows a distinct difference for mean TAE in stable and unstable conditions, where the previous results without the correction in figure 3.18 shows little difference for ensemble members driven by the PBL scheme MYNN under these atmospheric conditions. Conditioning of TAE over WRF wind direction in figure 3.32 results in lower TAE performance over Northern winds and a slight increase in TAE performance over Easterly winds.

Ultimately the effects of the correction over the $\sigma_{TAE_{xy}}$ is shown in figure 3.33 where we can observe a consistent reduction for the marginal $\sigma_{TAE_{xy}}$ for all ensemble members. The average difference in $\sigma_{TAE_{xy}}$ before and after the correction amounts to $0.015 [m \cdot s^{-1}]$ or about 13% decrease compared to the uncorrected data. This can also be interpreted as a reduction in uncertainty for WRF mean annual wind speed by the introduction of the stability correction for ASCAT measurements.

Comparing the results for the interpolation error metrics with the WRF error metrics is not trivial due to the difference in definition. Specifically, Δ_A considers spatial averages while the TAE considers time averages. Although that is true, we observe that the mean difference for averages $\langle \Delta_A \rangle_t$ (figure 2.8) doesn't indicate neither the overestimation nor the underestimation of wind speeds (on average). This information can be compared with the marginal mean TAE (fig-

ures 3.13, 3.18, 3.21, 3.30, 3.31 and 3.32) that show instead an overestimation of ASCAT data. Therefore we can argue that the mean overestimation observed is not due to the interpolation procedure. Since we also observe a significant standard deviation for Δ_A ($0.04 [m \cdot s^{-1}]$), compared to the marginal standard deviation of TAE ($0.12 [m \cdot s^{-1}]$), we can argue that the overestimation or underestimation of wind speeds by interpolation is present and has an effect over the standard deviation of TAE. A more precise evaluation of this influence is not possible based only on these values due to the difference in definitions. The results for mean RVAR in figure 2.9 shows a underestimation of both higher and lower values for WRF wind speeds. This result can be taken into consideration when conditioning TAE over WRF wind speed in figures 3.13 and 3.30. Since the extremes are under sampled, the results for the conditions $4 < U_w \leq 6$ and $12 < U_w \leq 26$ may be affected. Again, the amplitude of this influence can't be estimated due to the difference between error metrics definition for interpolation errors and WRF errors.

A comparison with previous work is not trivial due to the differences in model setup, measurements, duration of simulations, height above mean sea level and error metrics definition. Nevertheless in Hahmann et al. (2015) a comparison between WRF simulations and buoy measurements reports a *relative bias* ($RB [\%]$, similar to NTAE) between $-2\% > RB > -4\%$ at the station FINO1 (at 90 m), with six different ensembles. This result is similar to what we've obtained for NTAE in figure 3.15.

In Karagali et al. (2018), the comparison between WRF simulations and ASCAT measurements at 10 m height results in $\langle TAE \rangle_{xy}$ estimated at $0.5 [m \cdot s^{-1}]$ for a larger offshore area than the area of interest analyzed in this thesis (figure 2.5), with their analysis being over North sea and a section of the Baltic sea. The model setup in the latter paper is similar to the one presented in this thesis, with two ensemble members using the MYNN and YSU PBL schemes respectively. Our results are generally smaller for marginal $\langle TAE \rangle_{xy}$, with values between $0.3 [m \cdot s^{-1}]$ and $0.45 [m \cdot s^{-1}]$ for MYNN driven ensembles, and $0.2 [m \cdot s^{-1}]$ for YSU-MM5-OSTIA-NOAH and $0.6 [m \cdot s^{-1}]$ for YSU-MM5-OSTIA-RUC (e.g. blue line in figure 3.13). Note that we instead observe $\langle TAE \rangle_{xy}$ at $\sim 0.5 [m \cdot s^{-1}]$ for the MYNN and YSU ensemble members under neutral conditions in figure 3.18 (purple line), a value very close to the one obtained in Karagali et al. (2018).

Lastly we note that a comparison between ASCAT measurements and buoy measurements in Verhoef and Stoffelen (2009) shows statistics analogous to marginal $\langle RE \rangle_{xy,t}$ and $\sigma_{RE,xy,t}$ (buoy - ASCAT) at $-0.19 [m \cdot s^{-1}]$ and $1 [m \cdot s^{-1}]$ respectively. This means that if these statistics are valid for the entire selected area in the North sea (figure 2.5), the marginal mean RE shown in figure 3.9 will lower by $0.19 [m \cdot s^{-1}]$ when comparing WRF data to the buoy data. The standard deviation shown in latter paper is significantly lower than the marginal

$\sigma_{RExy,t}$ in figure 3.10 ($\sim 60\%$ of the values found in this thesis), meaning that the WRF model introduces a significant standard deviation when compared to measurements.

CHAPTER 5

Conclusions

Throughout this thesis we've analyzed different WRF simulations against ASCAT measurements for a given selected area of the North Sea. The interpolation procedure over space has been validated by defining and comparing two interpolation error metrics, the difference of averages (Δ_A) and ratio of variance ($RVAR$). These quantities have been obtained from the first non-central moment (spatial mean) and second central moment (spatial variance) of the distributions of wind speed respectively. To validate the interpolation, we compared how much these quantities change prior to and after interpolation. Given the interpolation error metrics, we've shown that information about their distributions can be used to infer how the interpolation acts on the data. Specifically, the temporal mean of Δ_A shows the overall overestimation or underestimation of either one of the wind distributions extremes, while the temporal standard deviation of Δ_A shows the magnitude of overestimation or underestimation of either wind speed distribution extreme. A analogous argument is true for the temporal mean and temporal standard deviation of $RVAR$, with the difference that $RVAR$ shows overestimation or underestimation of *both* extremes of the wind speed distribution. Having knowledge about the interpolation procedure, we can then compare the error metrics defined for the difference between WRF simulations and ASCAT measurements with the interpolation error metrics. Specifically, we observed that the average overestimation of WRF wind speeds is not due to interpolation (by comparing marginal $\langle TAE \rangle_{xy}$ and $\langle \Delta_A \rangle_t$) while $\sigma_{TAE_{xy}}$ is affected by the interpolation (comparing marginal $\sigma_{TAE_{xy}}$ and $\sigma_{\Delta_A t}$).

To compare WRF simulations and ASCAT measurements, two error metrics are defined. We've seen how two different formulations for the error metrics estimate a different characteristic of the WRF errors, with the raw error (RE) represent-

ing the correspondence between *individual* simulations and measurements and the time averaged error (*TAE*) represents the correspondence between *average* simulations and measurements. Different formulations are indeed possible, given the reader's objectives and destination for the error metric. Again we are interested in the distribution of the error metrics. We've specifically chosen to compare the mean and standard deviation of these distributions to check any systematic behaviour and to derive the uncertainty of the WRF simulations against the ASCAT data. Regarding uncertainty, we've proven that each error metrics shows a different uncertainty by comparing the standard deviations of *RE* and *TAE*. Therefore we suggest to clarify to which quantity the uncertainty in question refers to.

By presenting conditional statistics of the error metrics we've shown a more in-depth analysis of the WRF simulations. The results of this analysis can distinguish the sources of an undesired or anomalous behaviour of the simulations, such as poor performance of error metrics. Another use of conditional statistics can be found to highlight the differences in WRF schemes. We've presented three examples of conditional statistics. The analysis of *TAE* over wind speed revealed a monotonic relationship between this error metric and WRF wind speeds. The normalized TAE (NTAE, equation 3.4) conditioned over wind speed showed poor performance for the ensemble YSU-MM5-OSTIA-RUC. Other ensemble members sharing one or more schemes with the latter didn't share the poor performance, meaning that the combination of the schemes YSU, MM5 and/or RUC must cause the observed performance. The scheme MYJ was also found to show poor NTAE performance for lower wind speeds, while the sea surface temperature product OISST causes an increase in $\sigma_{TAE_{xy}}$ when used with the schemes MYNN and NOAH. Conditioning *TAE* over inverse Obukhov length showed unexpected results, with similar $\langle TAE \rangle_{xy}$ for stable and unstable conditions. The expectations was to observe a distinct difference in $\langle TAE \rangle_{xy}$ due to the assumption of neutral condition for the ASCAT data, meaning that these measurements should underestimate wind speeds over stable conditions and overestimate wind speeds over unstable conditions. This result eventually brought us to correct the ASCAT data to include stability effects. Conditioning *TAE* over WRF wind direction revealed again unexpected results, and a possible effect on wind speeds driven by the presence of coast uphill. A scheme to scheme comparison showed that the land surface scheme RUC is responsible for higher $\sigma_{TAE_{xy}}$ over northern winds. Note that at about NNE of the selected area (figure 2.5) we find a mountain range in Norway, possibly indicating a poor scheme performance over this terrain.

The correction of ASCAT data also enabled us to evaluate how much *TAE* was affected by the assumption of neutral atmospheric conditions for the ASCAT data. Among other differences, we observe a reduction in *TAE* standard deviation. This changed our perspective on the uncertainty of the WRF annual mean

wind speed, and assuming we evaluate uncertainty with the standard deviation, about 13% of the observed uncertainty of the WRF annual wind speed (compared to uncorrected data) is caused by the assumption of neutral conditions for the ASCAT data.

Bibliography

- Beljaars, A. and A. Holtslag, 1991: Flux parameterization over land surfaces for atmospheric models. *Journal of Applied Meteorology*, **30**(3), 327–341.
- Benjamin, S. G., G. A. Grell, J. M. Brown, T. G. Smirnova, and R. Bleck, 2004: Mesoscale weather prediction with the ruc hybrid isentropic-terrain-following coordinate model. *Monthly Weather Review*, **132**(2), 473–494.
- Berg, J., J. Mann, M. Kelly, and M. Nielsen, 2017: Micro meteorology for wind energy. Introduction to Micrometeorology DTU course notes.
- Copernicus, 2017: Pum for wind-global ocean l3 wind. <http://cmems-resources.cls.fr/documents/PUM/CMEMS-OSI-PUM-012-002.pdf>.
- Dee, D. P., S. M. Uppala, A. J. Simmons, P. Berrisford, P. Poli, S. Kobayashi, U. Andrae, M. A. Balmaseda, G. Balsamo, P. Bauer, P. Bechtold, and co authors., 2011: The era-interim reanalysis: Configuration and performance of the data assimilation system. *Quarterly Journal of the Royal Meteorological Society*, **37**(656), 553–597.
- Donlon, C. J., M. Martin, J. Stark, J. Roberts-Jones, E. Fiedler, and W. Wimmer, 2012: The operational sea surface temperature and sea ice analysis (ostia) system. *Remote Sensing of Environment*, **116**(Sp. Iss. SI), 140–158.
- EFKM, 2019: Danmarks storste havvindpark skal ligge i nordsen. <https://via.ritzau.dk/pressemeddeelse/danmarks-storste-havvindpark-skal-ligge-i-nordsoen?publisherId=9426318&releaseId=13569433>.

- EUMETSAT, 16 July 2015: *ASCAT product guide*. Eumetsat-Allee 1, D-64295 Darmstadt, Germany. <https://www.eumetsat.int>.
- Hahmann, A. N., C. L. Vincent, A. Pea, J. Lange, and C. B. Hasager, 2015: Wind climate estimation using wrf model output: method and model sensitivities over the sea. *International Journal of Climatology*, **35**(12), 3422–3439.
- Holtslag, M., B. W. A.A.M., and V. B. G. J.W., 2014: Estimating atmospheric stability from observations and correcting wind shear models accordingly. *Journal of Physics: Conference Series*, **555**(1), 012052.
- Hu, X.-M., P. M. Klein, and M. Xue, 2013: Evaluation of the updated ysu planetary boundary layer scheme within wrf for wind resource and air quality assessments. *J. Geophys.*, **118**(18), 10,490–10,505.
- Janji, Z. I., 1994: The step-mountain eta coordinate model: Further developments of the convection, viscous sublayer, and turbulence closure schemes. *Monthly Weather Review*, **122**(5), 927–945.
- Jimnez, P. A., J. Dudhia, J. F. Gonzlez-Rouco, J. Navarro, J. P. Montvez, and E. Garca-Bustamante, 2012: A revised scheme for the wrf surface layer formulation. *Monthly Weather Review*, **140**(3), 898–918.
- Karagali, I., A. N. Hahmann, M. Badger, C. B. Hasager, and J. Mann, 2018: New european wind atlas offshore. *Journal of Physics: Conference Series*, **1037**(5), 052007.
- Li, J. and Heap, 2008: *A Review of Spatial Interpolation Methods for Environmental Scientists*. Geoscience Australia Record, Sales Centre, Geoscience Australia, GPO Box 378, Canberra, ACT 2601.
- Mathworks, 2019a: griddata. <https://se.mathworks.com/help/matlab/ref/griddata.html>.
- Mathworks, 2019b: Nearest neighbor, bilinear, and bicubic interpolation methods. <https://se.mathworks.com/help/vision/ug/interpolation-methods.html>.
- MathWorks, 2019: Netcdf. <https://se.mathworks.com/help/matlab/ref/netcdf.html>.
- Monin, A. and A. Obukhov, 1954: Basic laws of turbulent mixing in the surface layer of the atmosphere. *Contrib. Geophys. Inst. Acad. Sci., USSR*(24), 163–187.
- Nakanishi, M. and H. Niino, 2006: An international journal of physical, chemical and biological processes in the atmospheric boundary layer. *Boundary-layer Meteorology*, **119**(2), 397–407.

- Nielsen, M., 2018: Planning and development of wind farms, dtu course 46200, course notes. Planning and development of wind farms DTU course notes.
- Noilhan, J. and S. Planton, 1989: A simple parameterization of land surface processes for meteorological models. *Monthly Weather Review*, **117**(3), 536–549.
- Obukhov, A., M., 1971: Turbulence in an atmosphere with a non-uniform temperature. *Boundary-layer Meteorology*, **2**(1), 7–29.
- Pleim, J., 2007: A combined local and nonlocal closure model for the atmospheric boundary layer. part i: Model description and testing. *Journal of Applied Meteorology and Climatology*, **46**(9), 1383–1395.
- Pope, S. B., 2000: *Turbulent Flows*. Cambridge University Press, 501.
- Reynolds, R. W., N. A. Rayner, T. M. Smith, D. C. Stokes, and W. Q. Wang, 2002: An improved in situ and satellite sst analysis for climate. *J. Geophys.* **15**(13), 1609–1625.
- Rosgaard, M. H., 2015: *Limited Area Forecasting and Statistical Modelling for Wind Energy Scheduling*. PhD thesis, Technical University of Denmark (DTU).
- Skamarock, C. W., B. J. Klemp, J. Dudhia, D. O. Gill, D. M. Barker, W. Wang, and J. G. Powers, 2008: A description of the advanced research wrf version 3. In *Tech. Rep. NCAR/TN-475+STR*. National Center for Atmospheric Research.
- Tewari, M., F. Chen, W. Wang, J. Dudhia, M. A. LeMone, K. Mitchell, M. Ek, G. Gayno, J. Wegiel, and R. H. Cuenca, 2004: . In *Implementation and verification of the unified noah land surface model in the WRF model*, of the American Meteorological Society, B., editor, volume 132, American Meteorological Society, 2165–2170.
- Troen, I. and E. L. Petersen, 1989: *European Wind Atlas*. Risø National Laboratory, Roskilde, Denmark, 656.
- UCAR, 2019: Wrf model physics options and references. http://www2.mmm.ucar.edu/wrf/users/phys_references.html.
- Verhoef, A. and A. Stoffelen, 2009: Validation of ascat 12.5-km winds. Ocean and Sea Ice SAF Technical Note SAF/OSI/CDOP/KNMI/TEC/RP/147, Ver. 1.2. [Online]. Available: www.knmi.nl/scatterometer/publications/pdf/ASCAT_validation_125.pdf.
- Wikipedia, 2015: List of offshore wind farms in the north sea. https://en.wikipedia.org/wiki/List_of_offshore_wind_farms_in_the_North_Sea.

Wikipedia, 2019: Netcdf. <https://en.wikipedia.org/wiki/NetCDF>.

Wilks, D. S., 2011: *Statistical methods in the atmospheric sciences, third edition*. Academic Press, The Boulevard, Langford Lane, Kidlington, Oxford, OX51GB, UK.

Witha, B., A. N. Hahmann, T. Sile, M. Drenkmper, Y. Ezber, E. G. Bustamante, J. F. Gonzalez-Rouco, G. Leroy, and J. Navarro, 2019: Report on wrf model sensitivity studies and specifications for the mesoscale wind atlas production runs : Deliverable d4.3. Technical report, NEWA - New European Wind Atlas.